Icarus 235 (2014) 170–186

Contents lists available at ScienceDirect

Icarus

journal homepage: www.elsevier.com/locate/icarus

Variations in the abundance of iron on Mercury's surface from MESSENGER X-Ray Spectrometer observations

Shoshana Z. Weider [a,*], Larry R. Nittler [a], Richard D. Starr [b], Timothy J. McCoy [c], Sean C. Solomon [a,d]

[a] Department of Terrestrial Magnetism, Carnegie Institution of Washington, Washington, DC 20015, USA
[b] Physics Department, The Catholic University of America, Washington, DC 20064, USA
[c] Department of Mineral Sciences, National Museum of Natural History, Smithsonian Institution, Washington, DC 20560, USA
[d] Lamont-Doherty Earth Observatory, Columbia University, Palisades, NY 10964, USA

ARTICLE INFO

Article history:
Received 24 December 2013
Revised 3 March 2014
Accepted 3 March 2014
Available online 11 March 2014

Keywords:
Mercury, surface
Spectroscopy

ABSTRACT

We present measurements of Mercury's surface composition from the analysis of MESSENGER X-Ray Spectrometer data acquired during 55 large solar flares, which each provide a statistically significant detection of Fe X-ray fluorescence. The Fe/Si data display a clear dependence on phase angle, for which the results are empirically corrected. Mercury's surface has a low total abundance of Fe, with a mean Fe/Si ratio of ~0.06 (equivalent to ~1.5 wt% Fe). The absolute Fe/Si values are subject to a number of systematic uncertainties, including the phase-angle correction and possible mineral mixing effects. Individual Fe/Si measurements have an intrinsic error of ~10%. Observed Fe/Si values display small variations (significant at two standard deviations) from the planetary average value across large regions in Mercury's southern hemisphere. Larger differences are observed between measured Fe/Si values from more spatially resolved footprints on volcanic smooth plains deposits in the northern hemisphere and from those in surrounding terrains. Fe is most likely contained as a minor component in sulfide phases (e.g., troilite, niningerite, daubréelite) and as Fe metal, rather than within mafic silicates. Variations in surface reflectance (i.e., differences in overall reflectance and spectral slope) across Mercury are unlikely to be caused by variations in the abundance of Fe.

1. Introduction

Prior to insertion of the MErcury Surface, Space ENvironment, GEochemistry, and Ranging (MESSENGER) spacecraft (Solomon et al., 2001) into orbit about Mercury, information on the elemental composition of Mercury's surface and interior was limited to constraints from Earth-based telescopic observations, the three Mercury flybys of Mariner 10 in 1974–1975, and the three Mercury flybys of MESSENGER in 2008–2009. Nonetheless, it has long been deduced that Mercury's high uncompressed density (~5.0 g/cm^3), the largest among the planets (Solomon, 2003), is a result of a high metal-to-silicate ratio. Models for Mercury's interior structure that include this constraint predict that the planet's core makes up ~80% of its total volume (Smith et al., 2012; Hauck et al., 2013). Several hypotheses for Mercury's formation have attempted to account for the high core fraction, either by accretion from precursor materials that were similarly enriched in metal phases (Lewis, 1973; Weidenschilling, 1978) or through an early high-temperature event that stripped away much of the planet's silicate portion, such as a giant impact (Benz et al., 1988) or evaporation in a hot solar nebula (Fegley and Cameron, 1987).

The data gathered by MESSENGER's X-Ray Spectrometer (XRS) and Gamma-Ray Spectrometer (GRS) since orbit insertion in March 2011 allow more definitive estimates of Mercury's surface composition to be made. Mercury's surface material is Mg-rich but Al- and Ca-poor compared with typical terrestrial and lunar rock types (Nittler et al., 2011; Evans et al., 2012; Peplowski et al., 2012b; Weider et al., 2012). Mercury's surface also has a high abundance of S, contained mainly in sulfide minerals (Nittler et al., 2011; Evans et al., 2012; Weider et al., 2012). In addition to the high S, measured K (Peplowski et al., 2011, 2012a) and Na (Evans et al., 2012; Peplowski et al., 2014) abundances indicate that Mercury is unlikely to be depleted in volatile elements compared with the other terrestrial planets. This finding has important ramifications for the giant impact and evaporation models for Mercury's formation. Although the loss of volatile species is a direct prediction of at least one giant impact model (Benz et al., 2007), the precise geochemical consequences of

* Corresponding author at: Department of Terrestrial Magnetism, Carnegie Institution of Washington, Washington, DC 20015, USA.
E-mail address: sweider@ciw.edu (S.Z. Weider).

http://dx.doi.org/10.1016/j.icarus.2014.03.002
0019-1035/

such an event are unresolved and are being actively investigated (e.g., Stewart et al., 2013).

Although Mercury has a high bulk abundance of Fe, the surface of the planet contains very little of the element. Both Earth-based telescopic (Vilas, 1985; Sprague et al., 2002) and MESSENGER flyby observations (McClintock et al., 2008) indicated, via the absence of a 1 μm absorption feature in surface reflectance spectra, that the crust has a very low ferrous Fe content, with less than ~6 wt% FeO in mafic silicates. Denevi et al. (2009) and Lawrence et al. (2010) proposed that Fe could instead be present on the surface within Fe–Ti oxides such as ilmenite ($FeTiO_3$). However, orbital XRS and GRS measurements (Nittler et al., 2011; Evans et al., 2012) have shown that the total Fe and Ti abundances on Mercury's surface are low (<1 wt% Ti; ~1–2 wt% Fe) and thus ruled out such a possibility.

It is now known that Mercury's surface exhibits a number of chemical heterogeneities. Large expanses of volcanic smooth plains in the northern lowlands (Head et al., 2011) and interior to the Caloris basin (Murchie et al., 2008) differ, in their concentration of Mg, Al, S, and Ca, from the older terrain that surrounds them (Weider et al., 2012). The distributions of K (Peplowski et al., 2012a) and Na (Peplowski et al., 2014) also vary over the northern hemisphere. Here we present the latest estimates for the Fe content of Mercury's surface from XRS data and investigate its spatial distribution.

2. Measuring Fe with the MESSENGER X-Ray Spectrometer

Through the technique of planetary X-ray fluorescence (XRF), the MESSENGER XRS data have been used to make quantitative estimates of major element abundances in Mercury's surface material (i.e., the uppermost ~100 μm). When incident X-rays from the Sun's corona impact Mercury's surface and induce ionization of individual atoms, characteristic X-ray photons are subsequently emitted that can be measured by the XRS on MESSENGER. The abundances of several major elements in surface material can be determined from the flux and energy of the fluorescent, as well as scattered solar, X-rays. The energy of the incident X-rays and the capabilities of the instrument detectors dictate which elements can be measured.

The MESSENGER XRS (Schlemm et al., 2007) has three gas-proportional counter (GPC) detectors that face the planet's surface and measure the XRF and scattered solar signals, as well as a separate Sun-facing Si-PIN photodiode detector that simultaneously measures the solar X-ray spectrum incident on the planet. All four detectors operate over an energy range of 1–10 keV. A "balanced-filter" approach (Starr et al., 2000) is employed whereby two of the GPC detectors have thin foils placed in front of them (one Mg, one Al) and the third detector has no filter. This arrangement allows the closely spaced XRF signals from Mg, Al, and Si, which cannot be resolved in the spectrum from a single detector, to be deconvolved. The resolution of the detectors is otherwise sufficient to resolve the spectral contributions of the heavier elements. The spatial resolution of the XRS measurements varies across the planet. The instrument's 12° field of view provides a "footprint" on the surface that varies greatly over the surface because of MESSENGER's eccentric orbit and the variable data integration periods of the instrument (Schlemm et al., 2007). The footprints range in size from <100 km across at high northern latitudes to >3000 km across at the south pole.

The binding energy of elements increases with their atomic number (Z), so higher-Z elements require the incidence of more energetic X-rays to be ionized. During relatively quiescent periods of solar activity ("quiet Sun"), XRS can detect Mg, Al, and Si XRF from Mercury's surface. During solar flare periods, when the solar X-ray flux increases at higher energies (i.e., "hardens"), XRF of heavier elements (e.g., S and Ca) can be detected; Fe XRF can be measured only during the strongest, and least common, solar flares. It is for this reason that it has taken longer to amass a substantial number of XRS Fe measurements than for the lower-Z elements (e.g., Weider et al., 2012). With these data we can now investigate the Fe abundance distribution over Mercury's surface in a statistically significant manner, although coverage at high spatial resolution in the northern hemisphere is still sparse.

3. Methodology

In this paper we present results from XRS measurements that were obtained from the start of MESSENGER's orbital mission through September 2013. We present data acquired during a total of 55 solar flares (see Table 1), from which statistically significant (<25% error) Fe abundances were derived from our forward modeling procedure (see Section 3.1). These flares all include at least one individual spectral integration for which the temperature of the emitting solar plasma is greater than 13.5 MK (the minimum temperature at which we have determined that XRS can reliably detect Fe XRF from Mercury's surface). We excluded (following Weider et al., 2012) flares for which the spectra showed evidence of substantial contamination from energetic electron events (e.g., Ho et al., 2011; Starr et al., 2012) or other charged particles (e.g., from coronal mass ejections), and those that had footprints on the planet's surface with an area larger than 10^7 km^2. Only one of the flares for which an Fe abundance was reported by Nittler et al. (2011) meets our criteria and is included in our data (flare 8 of Nittler et al., 2011; listed as flare 1 in Table 1); the result we present for this flare is from a new analysis of the data following the updated procedures we describe below.

3.1. Forward modeling

We used a forward modeling procedure (Nittler et al., 2011; Weider et al., 2012) to fit both the incident solar and planetary XRF spectra, and thus derive elemental abundances. Our method is based on the fundamental-parameters approach (e.g., Clark and Trombka, 1997; Nittler et al., 2001), by which the scattered solar spectrum and the theoretical fluorescence intensity of each element in a spectrum are calculated. The model requires several inputs that include the shape and magnitude of the incident spectrum, the viewing geometry, several atomic physics parameters, and the concentration of constituent elements in the target. The generated theoretical spectra are compared with the measured XRS GPC spectra to determine surface elemental abundances.

We fit the relatively low-resolution solar spectra from the solar monitor to characterize the emitting solar plasma (e.g., its temperature and elemental composition). We then employed the *CHIANTI* code (Dere et al., 1997) to generate equivalent, high-resolution model spectra, which were used in the forward modeling procedure. We analyzed only the XRF spectra from integrations that followed the temperature peak of the flare (as did Nittler et al., 2011 and Weider et al., 2012), because the plasma prior to the peak can have a multi-thermal nature (Garcia, 1994) and an isothermal regime is assumed in our modeling. Data from integrations toward the end of flares, when the plasma temperature is less than 13.5 MK (below which Fe XRF does not occur at a measureable level), were disregarded in this work.

Typically, the magnitude and spectral shape of detector backgrounds (generated from the interactions of galactic cosmic rays or solar energetic particles with the GPC detectors) remain constant on a timescale of tens of hours. The background magnitude, however, is slightly (10–15%) reduced when the spacecraft is close

Table 1
Solar flares used for Fe XRS data analysis.

Flare	Date	Start time (UTC)	Integration time (s)	Solar temperature (MK)	Mean incidence angle (°)	Mean emission angle (°)	Mean phase angle (°)
1	13 June 2011	03:53:20	1350	15.4	75.7	20.8	84.3
2	8 August 2011	22:00:39	400	16.3	76.2	12.0	78.9
3	1 September 2011	12:30:42	600	16.7	73.0	27.1	91.6
4	5 September 2011	00:16:35	900	14.9	75.4	21.7	86.8
5	6 September 2011	01:33:05	160	22.6	75.3	25.7	91.0
6	6 September 2011	01:43:45	520	21.1	75.4	26.3	91.8
7	6 September 2011	22:15:24	1000	22.8	65.8	17.0	78.1
8	8 September 2011	21:47:49	4900	16.6	77.9	15.2	82.6
9	9 September 2011	06:03:29	140	21.7	80.0	19.1	92.1
10	2 October 2011	08:49:04	340	16.4	21.3	57.7	77.8
11	18–19 October 2011	23:39:58	400	20.3	63.6	27.5	78.1
12	24 October 2011	08:11:52	300	14.7	53.5	47.9	97.9
13	26 October 2011	10:36:38	705	18.2	80.6	22.3	101.4
14	27 October 2011	12:40:24	1020	18.2	63.9	42.5	102.1
15	27 October 2011	20:24:51	713	19.7	78.0	28.7	103.4
16	27 October 2011	23:33:06	200	16.7	65.0	39.1	102.2
17	29 October 2011	22:53:59	684	18.2	83.9	11.1	87.1
18	29 October 2011	23:38:30	500	15.4	52.5	51.2	101.7
19	30 October 2011	14:57:45	900	16.9	68.6	42.2	103.7
20	31 October 2011	00:47:47	900	16.7	60.7	44.9	101.3
21	31 October 2011	14:57:34	1200	18.4	71.7	39.4	104.1
22	2 November 2011	22:04:48	260	16.5	85.4	5.6	85.4
23	3 November 2011	11:04:09	500	18.4	78.4	10.8	78.6
24	6 November 2011	01:02:16	900	15.6	57.9	46.7	100.2
25	5 December 2011	23:22:21	300	17.4	79.6	23.0	82.7
26	3 July 2012	05:34:09	1700	15.3	41.5	39.3	78.3
27	5 July 2012	06:52:44	800	15.7	52.3	26.4	78.2
28	10 July 2012	06:21:19	600	16.5	80.6	29.5	80.8
29	19 August 2012	18:07:27	1000	23.0	49.4	62.7	87.6
30	6 September 2012	15:16:47	280	15.8	26.8	51.9	78.3
31	12 September 2012	11:16:53	460	17.7	78.2	18.5	88.1
32	15 September 2012	11:15:29	400	18.2	79.2	18.9	90.3
33	19 September 2012	11:08:24	360	26.1	54.7	48.0	99.1
34	20 September 2012	05:21:29	240	29.5	21.7	59.4	75.9
35	23 October 2012	03:11:56	1300	21.7	63.1	42.7	102.0
36	13 November 2012	01:57:13	320	21.6	36.5	45.3	78.1
37	14 November 2012	03:58:15	400	16.1	55.4	48.0	99.9
38	21 November 2012	09:40:15	600	15.6	78.9	14.4	83.7
39	23 November 2012	23:07:12	400	19.9	73.8	15.2	80.2
40	28 November 2012	21:29:12	600	16.4	27.9	23.4	76.7
41	22 December 2012	06:24:32	400	16.6	25.6	54.9	77.3
42	15 February 2013	19:49:52	600	15.2	59.7	53.3	88.9
43	22 April 2013	10:23:53	200	18.1	27.4	53.6	76.9
44	7 May 2013	08:35:23	1160	20.5	50.5	28.5	78.0
45	10 May 2013	00:40:43	1067	19.5	42.7	35.8	78.1
46	18 May 2013	20:02:50	1000	15.8	69.5	48.4	89.8
47	18 May 2013	20:59:30	600	14.8	54.6	46.4	89.5
48	23 May 2013	14:40:50	400	16.9	28.9	52.2	77.3
49	3 July 2013	06:58:10	800	18.0	82.7	24.5	104.4
50	8 July 2013	01:16:10	400	15.8	52.4	35.0	84.8
51	15 August 2013	04:31:30	800	16.9	78.8	18.7	89.7
52	19 August 2013	07:22:50	683	18.7	25.2	55.3	77.1
53	27 September 2013	19:37:34	800	15.1	56.3	48.1	101.5
54	28 September 2013	14:53:34	800	16.4	76.8	29.9	103.3
55	29 September 2013	07:07:34	600	18.3	80.1	27.0	103.9

to periapsis and the planet blocks a larger portion of the cosmic ray flux. We derived the detector backgrounds by summing all the GPC spectra from the (Earth) day of the observation for which the field of view (FOV) did not include any part of the planet's surface. For the large flares analyzed here, the signal-to-noise ratio was generally sufficiently high that background changes caused by the planet's proximity were not significant. Therefore we simply scaled the background spectra, by integration time, to the XRF spectra as part of the fitting procedure. However, we have found that the spectral shape of the GPC detector backgrounds changes slightly during the peak output period of some, but not all, of the largest solar flares that occur when the planet is outside the instrument's FOV. In particular, an enhancement in the background continuum at energies of ~6–8 keV is often observed. The cause of this background change has not yet been identified, but it may be related to solar X-rays that are backscattered from Mercury's surface to the spacecraft and leak into the instrument at certain viewing geometries. It may be possible to explain difficulties in fitting the high-energy channels in our XRF spectra (see Section 3.3) with this atypical, enhanced background. The background we choose, however, does not markedly affect our overall chemical results.

3.2. Co-addition of spectra

For several of our 55 flares, the signal-to-noise ratio within the spectra from single XRS integration periods was insufficient to

provide accurate Fe abundance estimates (we excluded from our dataset Fe/Si measurements with relative errors of >25%). To mitigate this problem, we co-added all the spectra from the consecutive integrations for each flare. For consistency, we used this procedure even for the flares for which the Fe signal is strong. However, for three flares (flares 27, 44, and 45 in Table 1) with footprints in the northern hemisphere, i.e., where the spatial resolution of XRS was the highest, we divided the flares into several parts according to the terrain on which the footprints lay and analyzed the co-added spectrum for each of the sections (see Table 2).

Solar plasma temperature, and thus spectral shape, can change greatly over the course of a flare. It is therefore important to define an appropriate solar spectrum to use as an input to the forward modeling of these "co-added" spectra. We identified two options: (i) the *co-added spectrum* that is generated from the fitting of the equivalent "co-added" solar spectrum (i.e., from the addition of all the individual solar spectra from each integration), or (ii) the *weighted mean spectrum* that is derived by fitting the solar spectra for each integration separately and then calculating an average, which is weighted by the overall scale of each spectrum. The temperatures derived are similar in both cases, and the difference in the subsequent elemental weight ratio results is small, especially for the low-*Z* elements (the elemental results derived from the different solar models are mostly equal to within 10%; the variation increases to ~25% for Fe/Si from the weakest flares, for which the signal-to-background ratio is lowest and uncertainties in the solar model are greatest). We used the *weighted mean spectrum* for the solar input for all of our flare analyses because it more accurately captures the variation of the solar incident flux with time.

3.3. GPC spectral fitting

A non-linear χ^2 minimization routine was used to compare the measured XRF spectra with GPC spectra; parameter values were repeatedly varied until the best fit was obtained. The fitting parameters include the energy calibration and resolution of the three GPC detectors, as well as the elemental abundances (wt%) of Mg, Al, S, Ca, Ti, Cr, Mn, and Fe. Example co-added XRF spectra (for which the signals from all three GPC detectors have been summed) with best-fit theoretical spectra are shown in Fig. 1. Although the standard forward model provides a good fit to the spectrum across the entire energy range for some flares (e.g., 6 September 2012; Fig. 1a), for several others (e.g., 12 September 2012; Fig. 1b) the model lies below the measured spectrum at high energies (>7 keV). We found that the fit in this energy region can be greatly improved (Fig. 1c) by allowing the forward model to include fluorescent Ni (~7.5 keV) and Cu (~8.0 keV) signals. Such contaminating Cu signal is often observed in the GPC detectors and arises from interactions between the instrument collimators and charged particles that are commonly encountered in Mercury's orbit. The origin of possible Ni fluorescence, however, is less obvious. This signal may arise either as XRF from Mercury's surface or from detector materials. Alternatively, it is possible that the spectral misfit is due to an incorrect background subtraction, connected to the enhanced GPC backgrounds (in the 6–8 keV region) that are observed during some large flares (see Section 3.1). For these reasons, we do not infer or report Ni abundances for Mercury's surface.

It is important to note that including Ni and Cu in the forward model to improve the high-energy spectral fitting does not markedly affect the chemical results for the other elements. The potential impact is largest for Fe, because of the proximity of Fe and Ni XRF lines. However, a comparison with Fe abundances that are derived when Ni and Cu are excluded from the forward model indicates that only a minor (<15%) uncertainty is introduced to the derived Fe/Si ratios through their inclusion. This value is comparable to the overall uncertainty for a single Fe measurement (see Section 4.3). We therefore conclude that our results are not substantially affected by occasional high-energy spectral mismatches during large flares.

3.4. Limitations to the fundamental-parameters approach

3.4.1. Viewing geometry effects

The fundamental-parameters approach that underpins our forward modeling technique (Clark and Trombka, 1997; Nittler et al., 2001, 2011) is based on two separate assumptions. The first of these—that the analyzed surface is completely smooth and flat—is incorrect for the case of a planetary regolith, such as that at Mercury's surface. Surface topography occurs on a variety of spatial scales (e.g., grains, pebbles, hills), and the non-uniform size and shape of grains in Mercury's regolith can cause shadowing effects for the XRF measurements (e.g., Näränen et al., 2008), especially at large incidence, emission, and/or phase angles.

The ease with which fluorescent X-rays (at a particular energy) can escape from the surface, compared with that predicted by the fundamental-parameters approach, depends on the geometry of the observation. Several theoretical and experimental studies (e.g., Maruyama et al., 2008; Näränen et al., 2008; Parviainen et al., 2011; Weider et al., 2011) have shown that for observations made at a fixed emission angle, the intensity of XRF increases with increasing incidence angle; for measurements made at a fixed incidence angle, the intensity of XRF decreases with increasing emission angle. High phase angles (~90° or more) have also been shown to cause increased XRF flux (Okada, 2004). The magnitude of these geometry-dependent effects varies with the energy of the X-ray, the grain size, and the sample composition. We report elemental abundance results as ratios to Si, so the geometry of the observations becomes important when the energy of the

Table 2
Sections of flares 27, 44, and 45 (see Table 1) divided according to the terrains (as mapped by Denevi et al., 2013) sampled.

Flare	Terrain	Start time (UTC)	Integration time (s)	Solar temperature (MK)	Mean incidence angle (°)	Mean emission angle (°)	Mean phase angle (°)
27a	Smooth plains	06:52:44	200	17.2	48.4	30.3	78.1
27b	IcP-HCT*	06:56:04	600	15.1	53.5	25.0	78.1
44a	Northern volcanic plains	08:35:23	120	20.5	76.5	5.0	78.3
44b	Circum-Caloris smooth plains (north)	08:37:23	240	21.4	64.4	14.1	78.1
44c	Interior Caloris smooth plains	08:41:23	400	21.2	42.1	36.3	78.2
44d	Circum-Caloris smooth plains (south)	08:48:03	400	19.7	11.8	68.7	76.7
45a	Circum-Caloris smooth plains (northwest)	00:40:43	447	25.5	59.0	19.6	78.1
45b	Odin-type plains and Caloris rim	00:48:10	480	18.8	38.7	39.8	78.2
45c	Odin-type plains and Circum-Caloris smooth plains (southwest)	00:56:10	140	14.2	23.4	55.4	78.3

* IcP-HCT: Intercrater plains and heavily cratered terrain.

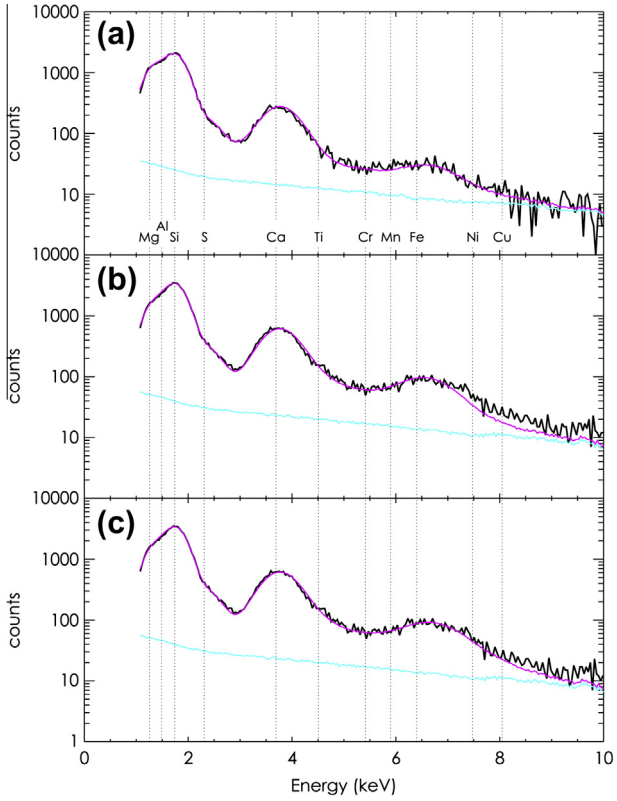

Fig. 1. MESSENGER XRS spectra (black, summed gas proportional counter spectra) and best-fit theoretical spectra (pink), illustrating the effect of varying Ni and Cu abundances in the forward modeling procedure. (a) 6 September 2012 flare (flare number 30 in Table 1), for which no Ni or Cu is required to provide a good fit to the spectrum at high energies (>7 keV); (b) 12 September 2012 flare (flare number 31 in Table 1), for which Ni and Cu are fixed at zero in the forward modeling procedure; and (c) fit to the 12 September 2012 flare spectrum when the abundances of Ni and Cu are allowed to float. A noticeable improvement to the fit at high energies is produced when Ni and Cu are adjustable parameters for fitting the 12 September flare spectrum. Cyan line indicates detector background.

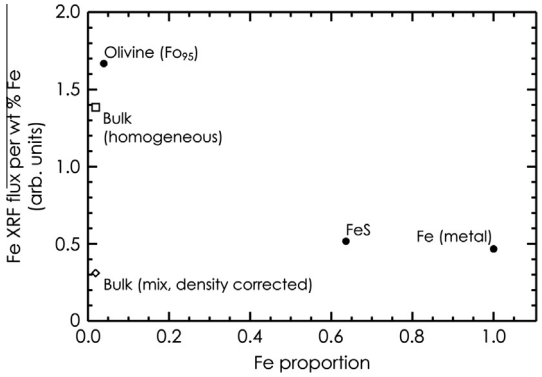

Fig. 2. The flux of fluorescent Fe X-rays from a specific amount of Fe in a sample depends on the phase in which it is contained (filled circles). The signal from forsteritic olivine is more than three times higher (per wt%) than from metal or sulfides. The open symbols show the calculated Fe XRF flux for a model mineralogy for Mercury's bulk surface, constructed from XRS and GRS measurements and petrologic modeling results (Stockstill-Cahill et al., 2012). The predicted flux from a homogeneous surface is greater than from a surface that is modeled as a mixture of several separate minerals.

element is substantially different (e.g., Fe) from that of Si. Indeed, we observe a phase-angle effect on our derived Cr/Si and Fe/Si ratios, to which we apply empirical corrections (see Section 4.1).

3.4.2. Mineral mixing effects

The second fundamental-parameters assumption—that the sample is chemically homogeneous—is also inaccurate when considering actual rocks that consist of different elements, contained in a variety of mineral species (e.g., Nittler et al., 2001). The mean free path of an X-ray varies with its energy (lower for lower-*Z* elements) and the material through which it is passing (greater attenuation by higher-*Z* elements). The relative proportions of the different chemical components in a sample, therefore, can be important if the regolith grains are larger than the typical X-ray mean free paths (<100 μm). Following the procedure of Nittler et al. (2001), we have investigated how mineral mixing corrections might affect our data, especially for Fe.

The level of Fe XRF we expect to observe, under given flare conditions, depends on the mineral phases that are the predominant carriers of Fe on Mercury's surface (see Section 5.1). If surface Fe were contained solely in FeS or in metal, the Fe XRF flux (for a given amount of Fe) should be about three times lower (see Fig. 2) than if it were present as FeO in a mafic silicate (e.g., olivine), given a typical solar flare excitation spectrum. This difference is an example of so-called XRF "matrix effects," whereby XRF flux depends non-linearly on all elements present in the sample. We constructed a model mineralogy for Mercury, for which the surface was assumed to be a mixture of olivine, pyroxene, plagioclase feldspar, oldhamite, troilite, and metallic Fe. We used average bulk compositions that have been determined from the XRS and GRS measurements (Evans et al., 2012; Peplowski et al., 2012a,b; Weider et al., 2012) and the petrologic modeling results of Stockstill-Cahill et al. (2012) to estimate relevant mineral compositions and relative proportions. We then calculated theoretical XRS GPC spectra (Fig. 3) for two separate cases: (i) the bulk composition is homogeneous throughout the surface, and (ii) the surface is heterogeneous and the 1.9 wt% Fe (from the GRS result of Evans et al., 2012) is split between its three likely mineral phases (0.1 wt% in FeO, 0.7 wt% in FeS, 1.1 wt% in Fe metal). Our results (see Fig. 2) show that when the surface is modeled as this specific mineral mixture, the flux of Fe XRF is ~4.5 times lower than for the homogeneous model. The difference reflects the lower XRF flux, per wt% Fe, for metal and sulfides than for silicates. It is also caused by the different densities of Fe metal (~8 g/cm^3), sulfide (~5 g/cm^3), and silicates (~3 g/cm^3); for a given amount of Fe, metal and sulfide grains have a smaller volume (and hence make up a smaller area in an XRS footprint) than silicate grains.

We define mineral mixing factors (following Nittler et al., 2001) as the ratios of the results we derive from our forward modeling for an assumed homogenous bulk composition to those derived from the mixed-mineral scenario. The magnitude of the factors varies for different elemental ratios; we derive correction factors of 1.11, 0.79, 0.70, 1.10, and 4.98 for Mg/Si, Al/Si, S/Si, Ca/Si, and Fe/Si, respectively, for our particular assumed mineralogy. If Mercury's regolith were made entirely of our modeled minerals with grain sizes substantially larger than ~100 μm, it would be necessary to correct our forward modeled results with these factors. We do not have a detailed knowledge of the nature of Mercury's regolith (e.g., grain size) and so it is impossible to ascertain if such corrections are necessary. This situation therefore introduces a systematic uncertainty in our methodology. For two reasons, however, we do not think that this uncertainty is as large as indicated by these factors: (i) Mercury's regolith should be dominated by fine-grained material after billions of years of steady impact bombardment (e.g., Langevin, 1997), and (ii) the uncorrected Al/Si, S/Si, and Ca/Si estimates from XRS agree well with the estimates from GRS. Nonetheless, the calculated correction factor for Fe/Si is large. The overall normalization and the true overall Fe/Si ratio could thus be much higher than we report, even if only a small fraction of the Fe

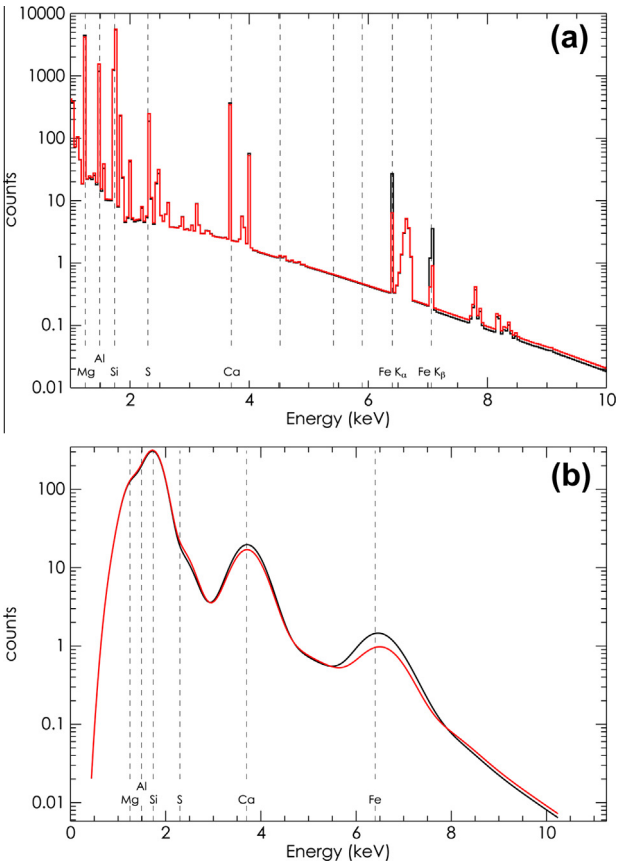

Fig. 3. (a) Theoretical X-ray spectra calculated for a solar temperature of 15 MK and a model Mercury mineralogy; the surface is modeled both as homogeneous (black) and as a mixture of several separate minerals (red). The spectra in (b) have been convolved through the XRS unfiltered GPC detector response. In both models, the Fe in Mercury's surface material (1.9 wt%; Evans et al., 2012) is assumed to be present as FeS or metal (i.e., with no ferrous Fe in silicates). The Fe (also Ca, to a lesser extent) flux is substantially lower for the mixed surface model, but for the lower-*Z* elements Mg, Al, Si, and S the opposite is true. Spectral peaks observed in (a) that do not correspond to X-ray K-lines are due to scattered solar X-rays at their ionized energies.

is contained in large metal or sulfide grains. In principle, apparent differences in derived Fe/Si ratios across Mercury's surface could reflect variations of some parameter (e.g., regolith grain size) other than composition. However, we observe spatially resolved variations in Fe/Si that correlate with other elements across geologic boundaries (see Section 4.4), a result that strongly suggests Fe/Si variability is dominated by intrinsic variations in composition rather than by some physical parameter. Therefore, even if the overall normalization remains uncertain (and our ratios are likely lower limits), relative differences among our derived Fe/Si ratios are likely to be robust.

4. Results

4.1. Phase-angle corrections

Our derived Mg/Si, Al/Si, S/Si, Ca/Si, and Ti/Si ratios are given in Table 3 and plotted as a function of the mean phase angle of the observation in Fig. 4. None of these ratios increase with phase angle, but in contrast, the derived Cr/Si and Fe/Si ratios clearly display a systematic increase with phase angle (Fig. 5). It should be noted that Mn/Si is also likely to be affected by a phase-angle effect, but the small number of Mn/Si values we have measured (Table 3) prevents the derivation of such a correlation. Our dataset thus represents the first time that phase angle effects have unambiguously been observed in planetary XRF data, although such an effect has been proposed to explain the discrepancy between X-ray and gamma-ray measurements of Fe/Si on the asteroid 433 Eros (Okada, 2002). A phase-angle effect had been predicted by many experimental and theoretical studies (e.g., Maruyama et al., 2008; Näränen et al., 2008; Parviainen et al., 2011; Weider et al., 2011), but these studies do not directly apply to the MESSENGER XRS observations in terms of the compositions and viewing geometries that are considered. We have therefore applied an empirical correction to the Cr/Si and Fe/Si data to account for the observed phase-angle effects, so that any true compositional heterogeneity in these elements on Mercury's surface can be investigated. To perform the corrections, we first determined the lines of best fit through the data (shown in Fig. 5a and c), to be

$$\mathrm{Cr/Si_{measured}} = (0.000375\alpha) - 0.0266 \quad (1)$$

$$\mathrm{Fe/Si_{measured}} = (0.002402\alpha) - 0.1556 \quad (2)$$

where $\mathrm{Cr/Si_{measured}}$ and $\mathrm{Fe/Si_{measured}}$ (mass percent ratios) are the results derived from our forward modeling and α is the mean phase angle (in degrees) of the observation. Although the theoretical increase with phase angle is closer to a cosine curve (with the increase in elemental ratio occurring at phase angles of more than ~60°), we have used linear fits to the data because they provide a good match to our results, and because we do not have any measurements at low phase angle (<60°). We divided each measurement by the value predicted by the relevant line of best fit to remove the phase-angle dependency, and then we multiplied by a normalization factor. The empirical nature of our corrections means that although the absolute normalizations are somewhat arbitrary, the relative differences among measurements are more robust.

Measurements made with phase angles <70° are least likely to be subject to the phase-angle effect and might provide a better measure of the absolute normalization. The measurements at lowest phase angle in our dataset are likely, therefore, to have the most accurate absolute values. However, several of the measurements at the lowest phase angles have footprints within a region of the planet (see Section 4.4) that has lower than average phase-angle-corrected Fe/Si ratios. Therefore, if we were to normalize all the data to the average of these measurements, a bias could be introduced. For this reason, and because of the large systematic uncertainty that is potentially connected to mineral-mixing corrections (Section 3.4.2), we used the mean value of the original data for the normalization (0.007 for Cr/Si; 0.055 for Fe/Si). The corrected Cr/Si and Fe/Si results are given in Table 3 and shown as a function of phase angle in Fig. 5b and d. The assigned errors are scaled in the same way as the data, i.e., no additional error has been propagated to account for the uncertainty in the phase-angle correction.

4.2. Correlating elemental ratios

The Mg/Si, Al/Si, S/Si, and Ca/Si ratios for our 55 analyzed flares are illustrated in Fig. 6 within the context of previously published XRS (Weider et al., 2012) and GRS (Evans et al., 2012; Peplowski et al., 2012b) results, all of which are broadly consistent. The new data we present here come mostly from large XRS footprints over Mercury's southern hemisphere, whereas the earlier results (from both XRS and GRS) are mainly from the northern hemisphere. Our results are in good agreement with the previously derived range in composition (Weider et al., 2012) for the intercrater plains and heavily cratered terrain (IcP-HCT) that surround the younger, smooth plains deposits (Trask and Guest, 1975). However, the majority of the new data also fall in a compositional range that overlaps with the northern plains. The agreement between the previous XRS datasets and the new data we present provides further evidence that Mercury's surface is likely dominated by high Mg-silicate minerals,

Table 3
Forward modeled elemental weight ratio results, with associated fitting errors, for the solar flare periods (as listed in Tables 1 and 2).

Flare	Mg/Si	Al/Si	S/Si	Ca/Si	Ti/Si	Cr/Si	Mn/Si	Fe/Si	Cr/Si (corrected)*	Fe/Si (corrected)*
1	0.380 ± 0.006	0.267 ± 0.006	0.051 ± 0.002	0.136 ± 0.002	–	–	–	0.058 ± 0.006	–	0.068 ± 0.007
2	0.393 ± 0.013	0.254 ± 0.015	0.061 ± 0.004	0.205 ± 0.006	–	–	–	0.061 ± 0.007	–	0.100 ± 0.012
3	0.443 ± 0.011	0.277 ± 0.011	0.069 ± 0.003	0.198 ± 0.004	–	–	–	0.092 ± 0.008	–	0.078 ± 0.007
4	0.427 ± 0.011	0.259 ± 0.012	0.061 ± 0.004	0.166 ± 0.004	–	–	–	0.045 ± 0.010	–	0.047 ± 0.010
5	0.429 ± 0.014	0.228 ± 0.013	0.068 ± 0.004	0.187 ± 0.004	–	–	–	0.075 ± 0.005	–	0.065 ± 0.005
6	0.435 ± 0.008	0.243 ± 0.008	0.076 ± 0.002	0.195 ± 0.003	0.012 ± 0.001	–	–	0.071 ± 0.004	–	0.060 ± 0.003
7	0.505 ± 0.005	0.253 ± 0.004	0.063 ± 0.001	0.135 ± 0.001	0.006 ± 0.001	–	0.008 ± 0.001	0.022 ± 0.001	–	0.038 ± 0.002
8	0.433 ± 0.004	0.261 ± 0.005	0.064 ± 0.001	0.156 ± 0.001	0.009 ± 0.001	0.003 ± 0.001	–	0.052 ± 0.003	0.005 ± 0.001	0.067 ± 0.004
9	0.475 ± 0.018	0.276 ± 0.017	0.092 ± 0.005	0.210 ± 0.005	0.010 ± 0.002	–	–	0.094 ± 0.008	–	0.079 ± 0.007
10	0.489 ± 0.006	0.318 ± 0.006	0.105 ± 0.003	0.221 ± 0.003	–	–	–	0.030 ± 0.005	–	0.053 ± 0.009
11	0.330 ± 0.010	0.250 ± 0.010	0.068 ± 0.002	0.184 ± 0.003	0.015 ± 0.001	–	–	0.035 ± 0.004	–	0.060 ± 0.007
12	0.500 ± 0.012	0.281 ± 0.013	0.087 ± 0.007	0.232 ± 0.006	–	–	–	0.128 ± 0.014	–	0.088 ± 0.010
13	0.429 ± 0.013	0.273 ± 0.012	0.077 ± 0.003	0.177 ± 0.004	0.016 ± 0.002	0.010 ± 0.002	–	0.081 ± 0.007	0.006 ± 0.001	0.051 ± 0.005
14	0.372 ± 0.006	0.266 ± 0.007	0.078 ± 0.003	0.216 ± 0.003	0.017 ± 0.002	–	–	0.096 ± 0.003	–	0.059 ± 0.002
15	0.310 ± 0.010	0.254 ± 0.011	0.063 ± 0.003	0.188 ± 0.003	0.011 ± 0.001	–	–	0.074 ± 0.003	–	0.044 ± 0.002
16	0.453 ± 0.016	0.230 ± 0.016	0.053 ± 0.006	0.173 ± 0.006	–	–	–	0.070 ± 0.010	–	0.043 ± 0.006
17	0.357 ± 0.015	0.236 ± 0.015	0.062 ± 0.004	0.169 ± 0.005	0.012 ± 0.002	–	–	0.065 ± 0.006	–	0.067 ± 0.006
18	0.405 ± 0.008	0.238 ± 0.009	0.073 ± 0.003	0.186 ± 0.003	0.010 ± 0.002	–	–	0.070 ± 0.006	–	0.044 ± 0.004
19	0.377 ± 0.011	0.262 ± 0.012	0.072 ± 0.004	0.185 ± 0.004	–	–	–	0.081 ± 0.009	–	0.048 ± 0.005
20	0.402 ± 0.006	0.279 ± 0.006	0.073 ± 0.002	0.202 ± 0.002	0.013 ± 0.002	–	–	0.089 ± 0.004	–	0.056 ± 0.002
21	0.406 ± 0.010	0.261 ± 0.010	0.066 ± 0.003	0.187 ± 0.003	0.011 ± 0.002	–	–	0.095 ± 0.004	–	0.055 ± 0.002
22	0.370 ± 0.012	0.215 ± 0.012	0.074 ± 0.004	0.184 ± 0.005	–	–	–	0.052 ± 0.006	–	0.058 ± 0.006
23	0.458 ± 0.009	0.240 ± 0.009	0.060 ± 0.002	0.161 ± 0.002	–	–	–	0.044 ± 0.004	–	0.072 ± 0.007
24	0.442 ± 0.007	0.282 ± 0.008	0.072 ± 0.003	0.208 ± 0.003	0.010 ± 0.002	–	–	0.102 ± 0.005	–	0.066 ± 0.003
25	0.428 ± 0.020	0.249 ± 0.019	0.060 ± 0.006	0.161 ± 0.006	–	–	–	0.051 ± 0.008	–	0.065 ± 0.011
26	0.520 ± 0.005	0.287 ± 0.006	0.086 ± 0.002	0.181 ± 0.002	–	–	–	0.038 ± 0.003	–	0.065 ± 0.006
27a	0.398 ± 0.008	0.333 ± 0.010	0.060 ± 0.003	0.180 ± 0.003	–	–	–	0.019 ± 0.004	–	0.033 ± 0.008
27b	0.522 ± 0.008	0.301 ± 0.009	0.057 ± 0.003	0.167 ± 0.003	–	–	–	0.029 ± 0.007	–	0.050 ± 0.011
28	0.482 ± 0.010	0.218 ± 0.009	0.092 ± 0.004	0.215 ± 0.004	–	–	–	0.062 ± 0.008	–	0.089 ± 0.011
29	0.350 ± 0.006	0.256 ± 0.007	0.077 ± 0.002	0.171 ± 0.002	0.010 ± 0.001	0.005 ± 0.001	0.002 ± 0.001	0.042 ± 0.002	0.005 ± 0.001	0.042 ± 0.002
30	0.485 ± 0.010	0.290 ± 0.010	0.069 ± 0.004	0.173 ± 0.004	–	–	–	0.037 ± 0.007	-	0.064 ± 0.012
31	0.376 ± 0.010	0.256 ± 0.010	0.062 ± 0.003	0.158 ± 0.003	0.010 ± 0.001	0.006 ± 0.001	–	0.066 ± 0.004	0.001 ± 0.001	0.065 ± 0.003
32	0.353 ± 0.013	0.275 ± 0.014	0.061 ± 0.004	0.151 ± 0.004	–	–	–	0.066 ± 0.008	–	0.059 ± 0.007
33	0.408 ± 0.010	0.218 ± 0.009	0.078 ± 0.003	0.200 ± 0.003	0.015 ± 0.001	–	–	0.058 ± 0.003	–	0.039 ± 0.002
34	0.351 ± 0.007	0.252 ± 0.007	0.094 ± 0.003	0.215 ± 0.002	0.016 ± 0.001	0.004 ± 0.001	–	0.024 ± 0.002	0.014 ± 0.003	0.049 ± 0.004
35	0.356 ± 0.009	0.267 ± 0.010	0.084 ± 0.004	0.257 ± 0.003	0.021 ± 0.002	0.011 ± 0.001	–	0.089 ± 0.003	0.006 ± 0.001	0.055 ± 0.002
36	0.419 ± 0.005	0.249 ± 0.006	0.091 ± 0.002	0.201 ± 0.002	0.010 ± 0.001	0.003 ± 0.001	–	0.030 ± 0.002	0.007 ± 0.002	0.052 ± 0.004
37	0.535 ± 0.008	0.279 ± 0.009	0.074 ± 0.003	0.207 ± 0.003	–	–	–	0.085 ± 0.005	–	0.055 ± 0.003
38	0.391 ± 0.008	0.266 ± 0.009	0.063 ± 0.003	0.161 ± 0.003	–	–	–	0.047 ± 0.007	–	0.057 ± 0.008
39	0.592 ± 0.014	0.191 ± 0.012	0.124 ± 0.004	0.230 ± 0.004	0.010 ± 0.002	–	–	0.036 ± 0.006	–	0.053 ± 0.009
40	0.434 ± 0.004	0.292 ± 0.005	0.086 ± 0.002	0.192 ± 0.002	–	–	–	0.031 ± 0.003	–	0.060 ± 0.007
41	0.355 ± 0.006	0.321 ± 0.007	0.102 ± 0.003	0.230 ± 0.003	–	–	–	0.029 ± 0.004	–	0.052 ± 0.008
42	0.473 ± 0.007	0.304 ± 0.009	0.082 ± 0.004	0.206 ± 0.004	–	–	–	0.074 ± 0.010	–	0.070 ± 0.009
43	0.412 ± 0.009	0.237 ± 0.009	0.079 ± 0.003	0.162 ± 0.003	–	–	–	0.021 ± 0.004	–	0.040 ± 0.008
44a	0.350 ± 0.014	0.276 ± 0.015	0.035 ± 0.004	0.112 ± 0.003	–	–	–	0.018 ± 0.003	–	0.030 ± 0.005
44b	0.326 ± 0.007	0.247 ± 0.007	0.051 ± 0.002	0.129 ± 0.002	–	–	–	0.018 ± 0.002	–	0.031 ± 0.004
44c	0.244 ± 0.004	0.304 ± 0.005	0.050 ± 0.002	0.151 ± 0.001	0.010 ± 0.001	–	–	0.013 ± 0.002	–	0.022 ± 0.003
44d	0.398 ± 0.005	0.271 ± 0.005	0.079 ± 0.002	0.186 ± 0.002	–	–	–	0.016 ± 0.002	–	0.030 ± 0.004
45a	0.429 ± 0.007	0.230 ± 0.007	0.080 ± 0.002	0.192 ± 0.002	0.013 ± 0.001	0.003 ± 0.001	0.006 ± 0.001	0.028 ± 0.002	0.008 ± 0.002	0.048 ± 0.003
45b	0.436 ± 0.005	0.248 ± 0.005	0.073 ± 0.002	0.169 ± 0.002	–	–	0.005 ± 0.001	0.015 ± 0.002	–	0.026 ± 0.004
45c	0.444 ± 0.006	0.261 ± 0.006	0.089 ± 0.002	0.182 ± 0.002	–	–	–	0.019 ± 0.003	–	0.032 ± 0.006
46	0.410 ± 0.007	0.307 ± 0.008	0.072 ± 0.002	0.189 ± 0.003	–	–	–	0.055 ± 0.003	–	0.050 ± 0.003
47	0.461 ± 0.006	0.248 ± 0.006	0.063 ± 0.002	0.160 ± 0.002	–	-	–	0.062 ± 0.003	–	0.057 ± 0.003
48	0.513 ± 0.008	0.295 ± 0.009	0.072 ± 0.003	0.170 ± 0.003	–	–	–	0.030 ± 0.005	–	0.055 ± 0.009
49	0.705 ± 0.035	0.271 ± 0.031	0.083 ± 0.009	0.178 ± 0.009	0.016 ± 0.005	0.024 ± 0.005	–	0.126 ± 0.017	0.013 ± 0.003	0.073 ± 0.010
50	0.340 ± 0.009	0.313 ± 0.011	0.078 ± 0.004	0.212 ± 0.004	0.014 ± 0.002	–	–	0.052 ± 0.009	–	0.059 ± 0.010
51	0.444 ± 0.014	0.245 ± 0.015	0.053 ± 0.004	0.145 ± 0.004	–	–	–	0.054 ± 0.006	–	0.050 ± 0.006
52	0.483 ± 0.005	0.237 ± 0.005	0.090 ± 0.002	0.185 ± 0.002	–	0.002 ± 0.001	–	0.020 ± 0.002	0.005 ± 0.002	0.038 ± 0.004
53	0.439 ± 0.011	0.271 ± 0.011	0.056 ± 0.004	0.165 ± 0.005	–	–	–	0.063 ± 0.013	–	0.039 ± 0.008
54	0.406 ± 0.014	0.258 ± 0.016	0.061 ± 0.005	0.162 ± 0.005	–	–		0.067 ± 0.009	–	0.040 ± 0.005
55	0.432 ± 0.017	0.240 ± 0.015	0.054 ± 0.005	0.158 ± 0.004	–	0.003 ± 0.002	–	0.085 ± 0.007	0.002 ± 0.001	0.050 ± 0.004

* Cr/Si and Fe/Si results corrected for the phase-angle effect (see Section 4.1).

feldspars, and sulfide phases such as oldhamite (CaS) and niningerite (MgS).

The phase-angle-corrected Fe/Si values are plotted as a function of Mg/Si, Al/Si, S/Si, and Ca/Si in Fig. 7. Although the new mean XRS and the earlier GRS (Evans et al., 2012) Fe/Si values (0.06 ± 0.02 and 0.08 ± 0.01, respectively) are consistent at the one-standard deviation (1σ) level, the GRS estimate is offset toward the higher end of the XRS dataset. This mismatch could indicate either that the southern hemisphere has less Fe than the northern hemisphere, or that there is a systematic uncertainty in one, or both, of the datasets. For example, only a small contribution from the mineral mixing effects we discuss in Section 3.4, or a change to the absolute phase-angle normalization (see Section 4.1), would be required to account for the difference.

Ti/Si, Cr/Si, and Mn/Si values can also be derived from the forward modeling of some of the flare XRF spectra we have analyzed

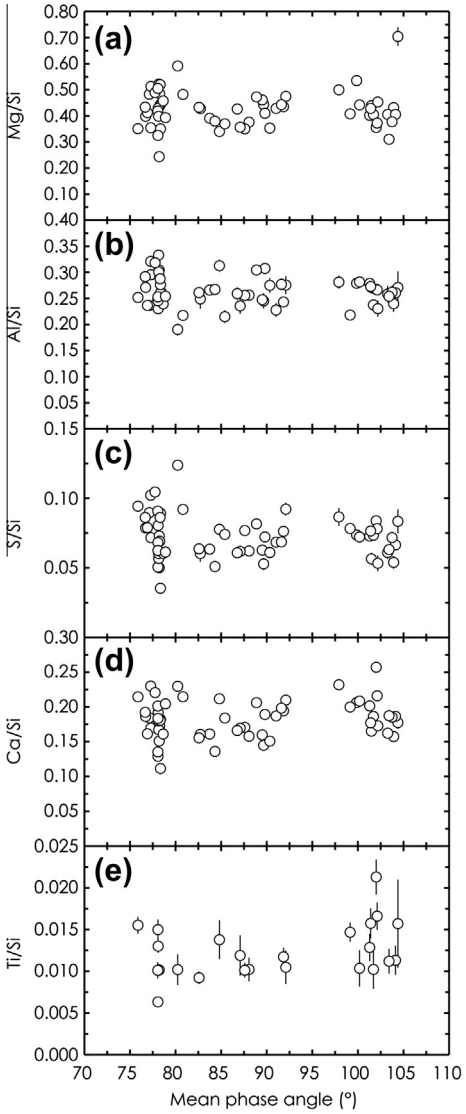

Fig. 4. (a) Mg/Si, (b) Al/Si, (c) S/Si, (d) Ca/Si, and (e) Ti/Si forward modeling results for the 55 solar flares, plotted as a function of the mean phase angle of each observation.

(Table 3). The number of reliable measurements we obtain for these high-Z and minor elements is limited by the poor XRF counting statistics. Variations in their abundances across the surface are therefore difficult to determine with confidence. Mean values for each of these ratios, however, are consistent with the estimates that were previously provided by Nittler et al. (2011). We use the values given in Table 3 to calculate mean Ti/Si, Cr/Si (corrected for the phase-angle effect), and Mn/Si ratios (with standard deviations) of 0.012 ± 0.003, 0.005 ± 0.002, and 0.004 ± 0.003, respectively.

4.3. Errors in derived Fe/Si ratios

The errors we quote for the elemental ratios of individual flare measurements (Table 3) were derived with the non-linear spectral fitting procedure and are based on the counting statistics and goodness of fit. For several reasons, however, the true errors are likely to be somewhat larger. Systematic uncertainties may arise from such factors as: (i) the solar spectra fitting procedure, (ii) the choice of GPC detector background, (iii) the empirical phase-angle corrections, (iv) possible effects of averaging the viewing geometry for large footprints, and (v) mineral mixing effects.

We can assess the overall uncertainty on individual measurements by comparing the results from overlapping XRF footprints. In an ideal situation, separate measurements of the same region should give the same result; we therefore calculated the degree of areal overlap and difference in measured Fe/Si for all pairs of our 55 flare footprints. Our "overlap factor" (OF) is defined as

$$\mathrm{OF} = (A_{ol})^2/(A_1 \times A_2) \tag{3}$$

where A_1 and A_2 are the surface areas of two overlapping footprints and A_{ol} is the area of their overlap.

A plot of the difference in measured Fe/Si (in units of the standard deviation) versus OF for all of the footprint pairs is shown in Fig. 8a. The level of agreement between any two measurements tends to increase as the degree of overlap between their footprints increases. This trend indicates that repeated measurements for a specific area are reproducible and that much of the variability we observe in the Fe/Si dataset is due to real chemical heterogeneity on Mercury's surface. However, several pairs of footprints with OF values of >0.8 have Fe/Si ratios that differ by more than 2σ, which indicates that the fitting errors we derived for individual flare measurements are smaller than the true errors.

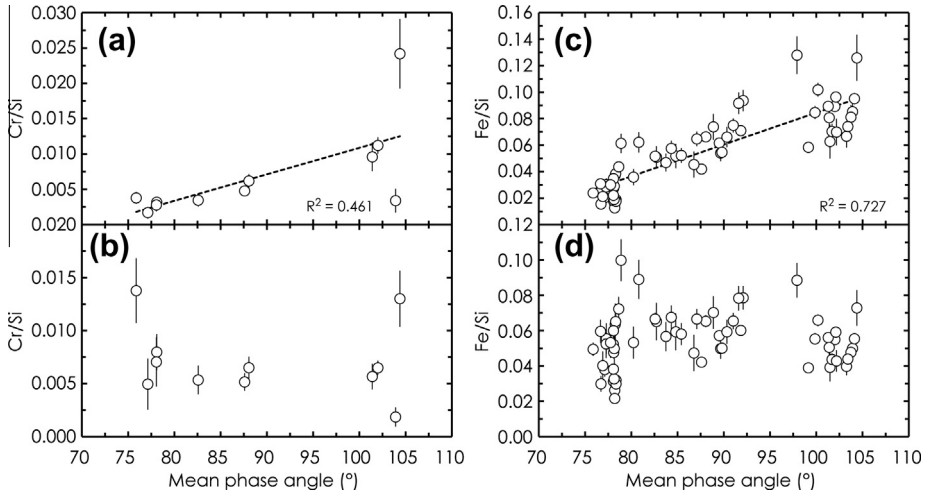

Fig. 5. (a) Cr/Si and (c) Fe/Si forward modeling results for the 55 solar flares, plotted as a function of the mean phase angle of each observation. Both element ratios display a clear correlation with phase angle. The line of best fit through the data is shown in both cases. The data, corrected for phase angle, are shown in (b and d) for Cr/Si and Fe/Si, respectively. Details of the phase-angle correction are given in Section 4.1.

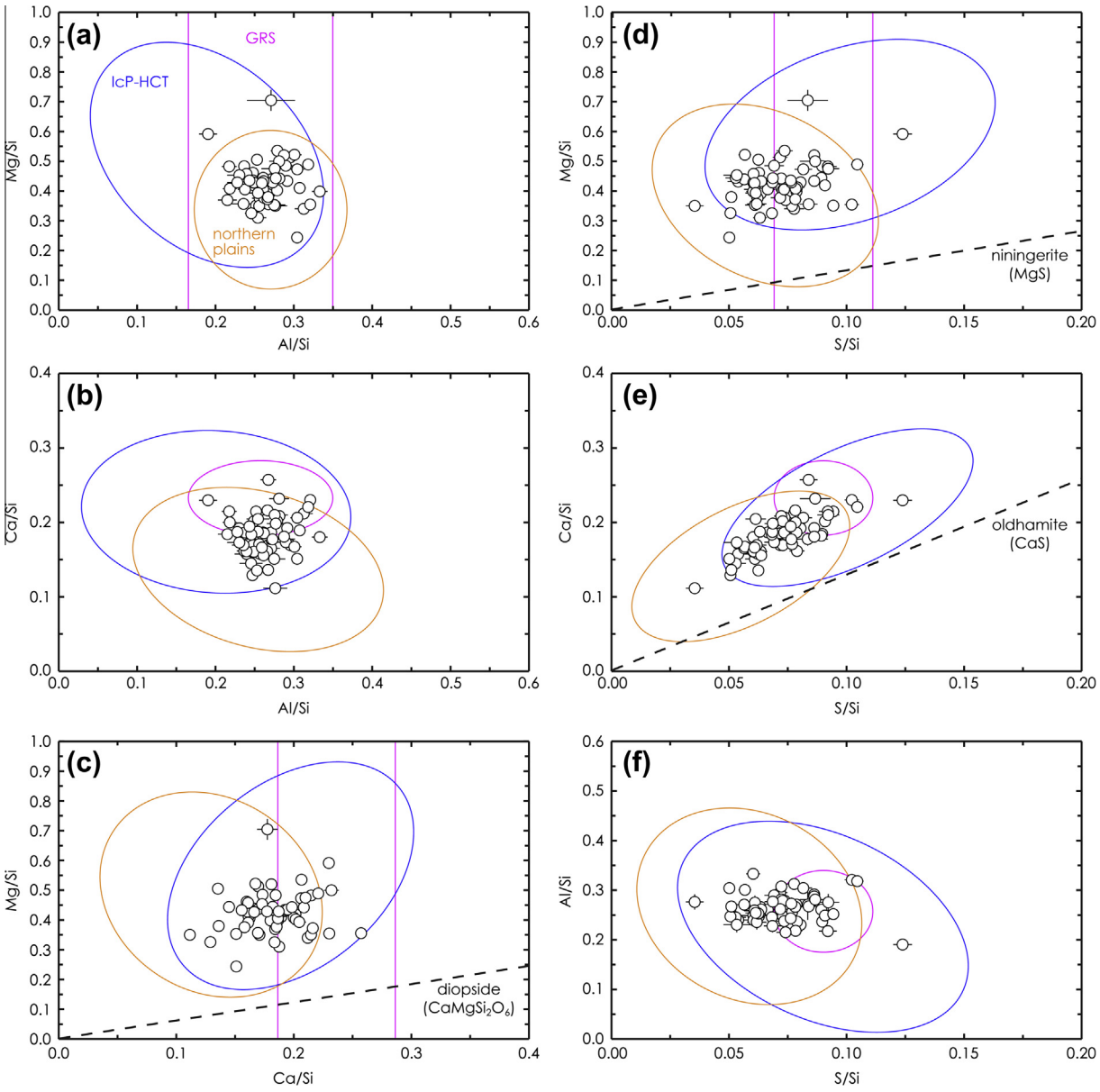

Fig. 6. Forward modeled Mg/Si, Al/Si, S/Si, and Ca/Si elemental weight ratios. (a) Mg/Si versus Al/Si; (b) Ca/Si versus Al/Si; (c) Mg/Si versus Ca/Si; (d) Mg/Si versus S/Si; (e) Ca/Si versus S/Si; and (f) Al/Si versus S/Si. Ellipses indicate the composition ranges from previously published XRS data (Weider et al., 2012) for the northern plains (orange) and the intercrater plains and heavily cratered terrain (ICP-HCT; blue). Also shown are the 1σ error ranges for GRS measurements of Mercury's northern hemisphere (pink) from Evans et al. (2012) and Peplowski et al. (2012b). Dashed lines denote mixing trends between (c) pure diopside ($CaMgSi_2O_6$) and a Ca-, Mg-free composition, (d) pure niningerite (MgS) and a Mg-, S-free composition, and (e) pure oldhamite (CaS) and a Ca-, S-free composition.

We show the same data in Fig. 8b, but with an additional 10% relative uncertainty added to each of the flare measurements. Because of the incorporation of larger relative uncertainties in this figure, all pairs of footprints with OF > 0.6 have Fe/Si ratios that agree to within 2σ. We therefore infer that the magnitude of additional systematic uncertainties in our Fe/Si measurements (excluding possible mineral mixing effects) is no more than ~10%, and we conclude that this value is close to the intrinsic uncertainty associated with the individual Fe/Si measurements.

4.4. Mapping Fe/Si

Because repeated measurements of the same region give reproducible results (see previous section), we have combined the data from the 55 flares to construct a map of Fe/Si across Mercury's surface (Fig. 9a) by assigning the derived values from our forward modeling to each flare footprint. The size and shape of the footprints vary across the surface, because they depend on the spacecraft altitude and the instrument pointing geometry at the time of the observation, as well as on the integration period; smaller footprints are generally located in the northern hemisphere. We divided the surface into $0.25^\circ \times 0.25^\circ$ pixels and assigned to each pixel a weighted average Fe/Si value of all the footprints that overlap with it, which we calculate as

$$\left(\frac{\mathrm{Fe}}{\mathrm{Si}}\right)_{\mathrm{av}} = \frac{\sum_{i=1}^{N} w_i \left(\frac{\mathrm{Fe}}{\mathrm{Si}}\right)_i}{\sum_{i=1}^{N} w_i} \tag{4}$$

where N is the number of footprints overlapping with a given pixel, and w_i the weighting factor, defined as

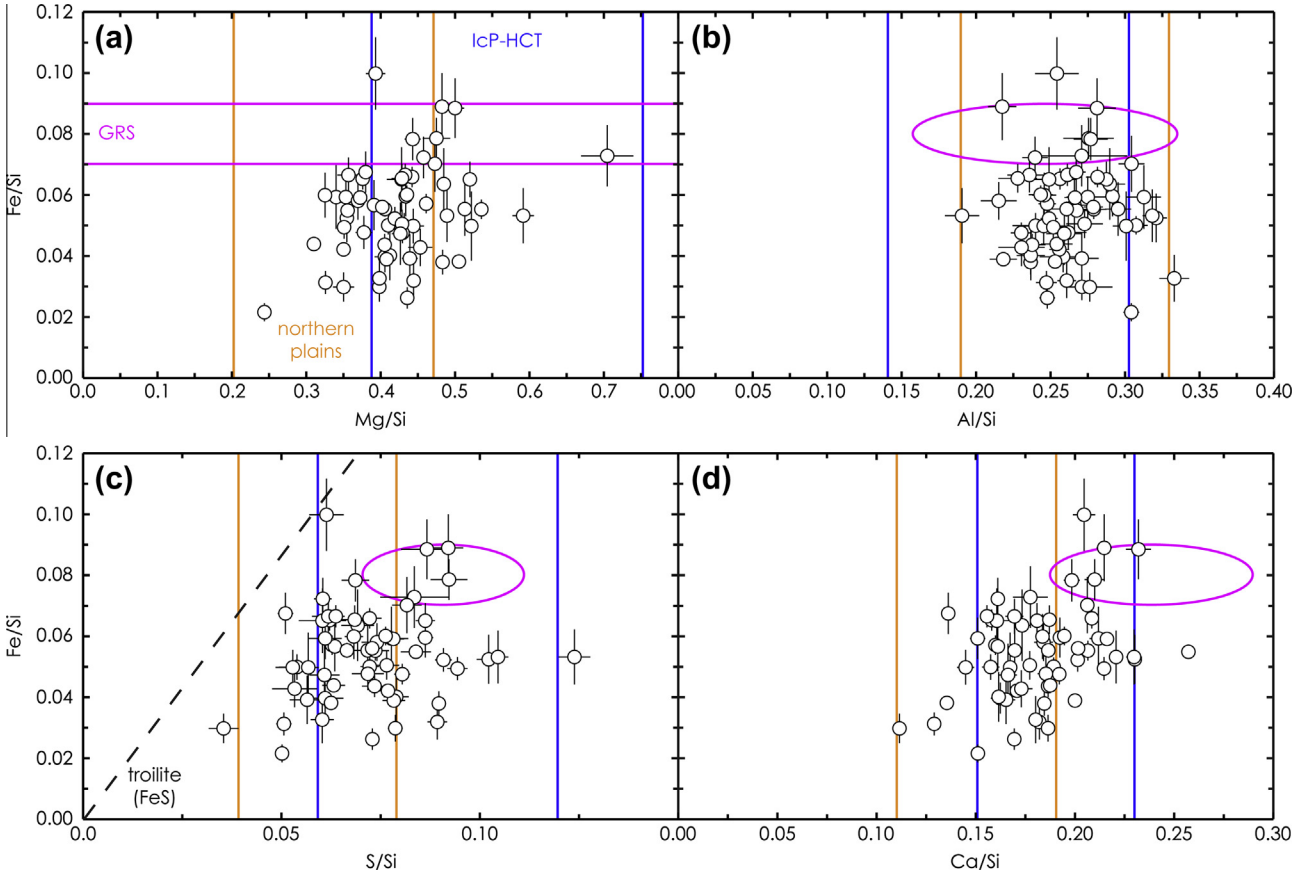

Fig. 7. Forward modeled Fe/Si (corrected for phase-angle effect; see Section 4.1), Mg/Si, Al/Si, S/Si, and Ca/Si elemental weight ratios. (a) Fe/Si versus Mg/Si; (b) Fe/Si versus Al/Si; (c) Fe/Si versus S/Si; and (d) Fe/Si versus Ca/Si. Colored lines indicate the composition ranges from previously published XRS data (Weider et al., 2012) for the northern plains (orange) and the intercrater plains and heavily cratered terrain (ICP-HCT; blue). Also shown are the 1σ error ranges for GRS measurements of the elemental composition of Mercury's northern hemisphere (pink) from Evans et al. (2012) and Peplowski et al. (2012b). The dashed line in (c) denotes the mixing trend between pure troilite (FeS) and an Fe-, S-free composition.

$$w_i = \frac{1}{A_i \times \sigma_i^2} \tag{5}$$

where A_i is the surface area of the footprint and σ_i is the error of the Fe/Si measurement from flare i. The average is therefore weighted to favor data from footprints with smaller areas (since they are more likely to sample a geologically well-defined region on the surface) and to measurements with smaller analytical errors. Similarly, the uncertainty for a given pixel is defined as a weighted standard error of the mean for the individual Fe/Si measurements:

$$\sigma = \sqrt{\frac{\sum_{i=1}^{n} w_i \left(\left(\frac{\mathrm{Fe}}{\mathrm{Si}}\right)_i - \left(\frac{\mathrm{Fe}}{\mathrm{Si}}\right)_{\mathrm{av}}\right)^2}{(N-1)\sum_{i=1}^{N} w_i}} \tag{6}$$

When only a single XRS footprint overlaps with a pixel, the pixel is assigned the measured Fe/Si and an error that is based on the analytical uncertainty of the measurement and the estimated intrinsic uncertainty of 10% (see previous section).

Our mapping procedure is essentially non-uniform image smoothing, so direct comparisons of the Fe/Si map with other parameters (e.g., reflectance, phase angle) require that these other data be smoothed in an identical fashion. To produce a smoothed map of phase angle (i.e., the phase angle for each of the Fe/Si measurements), as shown in Fig. 9d, we substituted phase angle measurements for $(\mathrm{Fe/Si})_i$ in Eq. (4) (the values for w_i, however, are still based on the Fe/Si measurements). We also similarly derived an "effective resolution" map (Fig. 9b) by substituting the equivalent diameter of each flare footprint (under the simplifying assumption that each footprint is circular) for the Fe/Si values in Eq. (4). To produce smoothed reflectance maps (Fig. 9c and e; see Section 5.2), we took the average value for the given spectral parameter over all pixels in the i^{th} Fe/Si measurement footprint and used these mean values in lieu of $(\mathrm{Fe/Si})_i$ in Eq. (4) (with values for w_i still based on the Fe/Si measurements).

The full map containing data from all 55 flares is displayed in Fig. 10a. Fe/Si values for pixels with more overlapping footprints have greater accuracy because of the averaging procedure. For comparison, the maps in Fig. 10b and c show only those pixels that have data from at least two or three overlapping footprints, respectively. Although in Section 4.3 we concluded that the intrinsic relative error on a single Fe/Si measurement is ~10%, the uncertainty associated with a given map pixel can be much smaller because of the effect of averaging several overlapping results. Subtle differences in Fe/Si over larger areas are therefore discernable, although the sharp compositional boundaries in the southern hemisphere (apparent in Fig. 10) are artifacts of the mapping procedure. To ascertain the statistical significance of variations in Fe/Si across Mercury's surface, we generated significance maps that illustrate pixels for which the Fe/Si values are significantly different from the planetary average at 2-σ, 2.5-σ, and 3-σ levels (Fig. 11).

The Fe/Si map has good coverage but poor spatial resolution in the southern hemisphere (see Fig. 9b), whereas the northern hemisphere of Mercury remains largely unmapped in Fe/Si from XRS results. It is difficult therefore to investigate whether heterogeneity in the distribution of Fe/Si across the surface of Mercury is related to the spatial variations of Mg/Si, Al/Si, S/Si, and Ca/Si that have

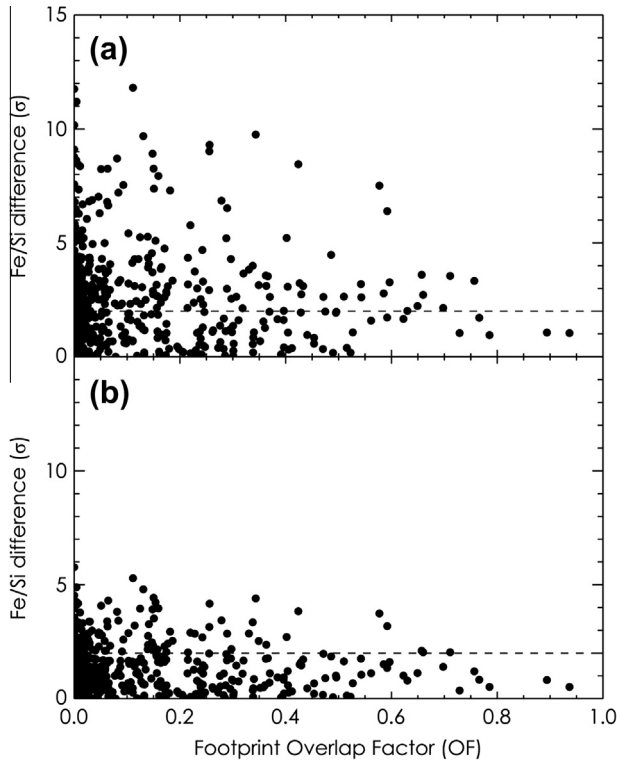

Fig. 8. (a) The difference in measured Fe/Si (expressed in numbers of standard deviations) versus the degree of spatial overlap for pairs of footprints from the 55 analyzed solar flares. The spread in measured Fe/Si decreases with increasing degree of footprint overlap, which indicates that repeated measurements for specific areas are generally reproducible and that much of the variability we observe in the Fe/Si dataset is the result of chemical heterogeneity on Mercury's surface. In (b) an additional 10% relative uncertainty has been propagated into each of the flare measurements.

previously been identified (Weider et al., 2012). Nonetheless, the few data we have for the northern hemisphere provide some evidence that the smooth plains deposits that have been sampled by XRS have significantly lower Fe/Si (Figs. 9 and 10) than the southern hemisphere average. In particular, data for the Caloris basin indicate that Mg/Si and Fe/Si are lower for the smooth plains within the Caloris basin than in the surrounding terrain (Table 2). If we assume that the northern volcanic plains (Head et al., 2011) also have a low Fe content, then the average Fe/Si ratio would be expected to be lower in the northern hemisphere than in the southern hemisphere, as there are few large deposits of smooth plains south of the equator (Denevi et al., 2013). However, such an outcome would enhance the mismatch between the XRS and GRS estimates of Fe/Si that we noted in Section 4.2, as the GRS has only sampled Mercury's northern hemisphere. Alternatively, the Fe content of the northern plains may be broadly similar to the southern hemisphere average we have derived. This may be the case if the Fe abundance is correlated with the S content (see Section 5.1), as we observe for heavily cratered terrain in the northern and southern hemispheres. Better coverage of the Fe/Si map in the northern hemisphere (i.e., observations during additional strong solar flares) is needed to address this issue more fully.

Two regions with slightly lower than average Fe/Si (red colors in Fig. 10 and blue in Fig. 11) can be seen in the southern hemisphere, centered near 30°S, −30°E and 30°S, +160°E. In addition, the region surrounding 50°S, 60°E has a somewhat higher Fe/Si ratio than average (yellow–green color in Fig. 10 and red in Fig. 11). Although the overall differences in the Fe contents of these regions are small, they can be resolved because of the large number of overlapping footprints and our ability to average several measurements. These heterogeneities appear to be significant at the 2-σ and 2.5-σ confidence levels, but they are less evident at the 3-σ level (Fig. 11).

To investigate whether the apparent heterogeneity in Fe/Si ratio is related to a residual phase-angle effect, we plotted the value for each pixel in the phase-angle map versus the Fe/Si value (Fig. 9f). We do not find a correlation, which indicates that the large-scale southern hemisphere heterogeneity in Fe/Si is not due to a residual phase-angle effect caused by an incorrect empirical correction. In addition, significant Fe/Si variations derived from measurements acquired during single flares (i.e., at constant phase angle) in the northern hemisphere (see Table 2) indicate differences in Fe/Si among geological units around the Caloris basin (Figs. 10 and 11) and correlate with other changes in composition (e.g., Mg/Si). We are therefore confident that the variations in Fe/Si that we observe reflect chemical heterogeneity on Mercury. The low-Fe/Si region near 30°S, 160°E in our map coincides with an area of high-reflectance smooth plains, which have color properties that are distinct from most other circum-Caloris plains and are more similar to plains interior to the basin. This pattern supports our earlier suggestion that Mercury's smooth plains deposits tend to have Fe/Si ratios that are lower than the average value for the southern hemisphere.

5. Discussion

5.1. Possible Fe-bearing mineral phases

It has long been known, from Earth-based telescopic observations (e.g., Vilas, 1985) as well as from MESSENGER flyby measurements (Robinson et al., 2008; McClintock et al., 2008), that Mercury's surface silicate minerals contain little or no FeO. The ubiquitous absence of a diagnostic absorption band at ~1 μm in reflectance spectra from Mercury's surface indicates that there is less than ~6 wt% FeO (~4.7 wt% Fe) in silicates (Vilas, 1988; Blewett et al., 2002). More recent comparisons of Mercury's spectra with those of low-Fe silicates indicate that this upper limit could be as small as ~0.5 wt% FeO (Klima et al., 2013). Our results confirm the earlier XRS and GRS observations (Nittler et al., 2011; Evans et al., 2012) that the total Fe content of Mercury's surface is low, at ~1.5 wt%. Furthermore, Mercury's low oxygen fugacity (between ~2.5 and ~6.5 log units below the iron-wüstite buffer; McCubbin et al., 2012; Zolotov et al., 2013), which has been inferred from the observed high S and low Fe contents, makes it likely that the majority of the Fe is present in a reduced form and is contained within non-silicate minerals.

Zolotov et al. (2013) showed that at the highly reduced conditions inferred for Mercury's mantle, the FeO content of silicates derived from partial melts would be lower (~0.03–0.8 wt%) than the equivalent Fe abundances indicated by the XRS and GRS measurements. Fe on Mercury's surface is therefore most likely present in sulfides and/or metal. Troilite (FeS), with a dark and red reflectance spectrum, has been proposed as a possible component of Mercury's surface material (e.g., Sprague et al., 1995; Blewett et al., 2013). However, the abundance of FeS is limited by the concentration of Fe we detect from XRS and by the weak correlation between Fe/Si and S/Si in our data (Fig. 5c). As such, it is more likely that Fe is largely contained either in metallic phases and/or as a minor component in other sulfide phases, such as niningerite (MgS), daubréelite ($FeCr_2S_4$), or djerfisherite ($K_6Na(Fe,Cu,Ni)_{25}S_{26}Cl$), which are thought to exist on Mercury's surface (Nittler et al., 2011; Weider et al., 2012). Although oldhamite (CaS) is likely to be a major sulfide phase on Mercury (Nittler et al., 2011; Weider et al., 2012), this mineral incorporates almost no Fe into its structure (e.g., McCoy, 1998; Mittlefehldt et al., 1998). If Fe is included only as a minor component in sulfide minerals and in its metallic

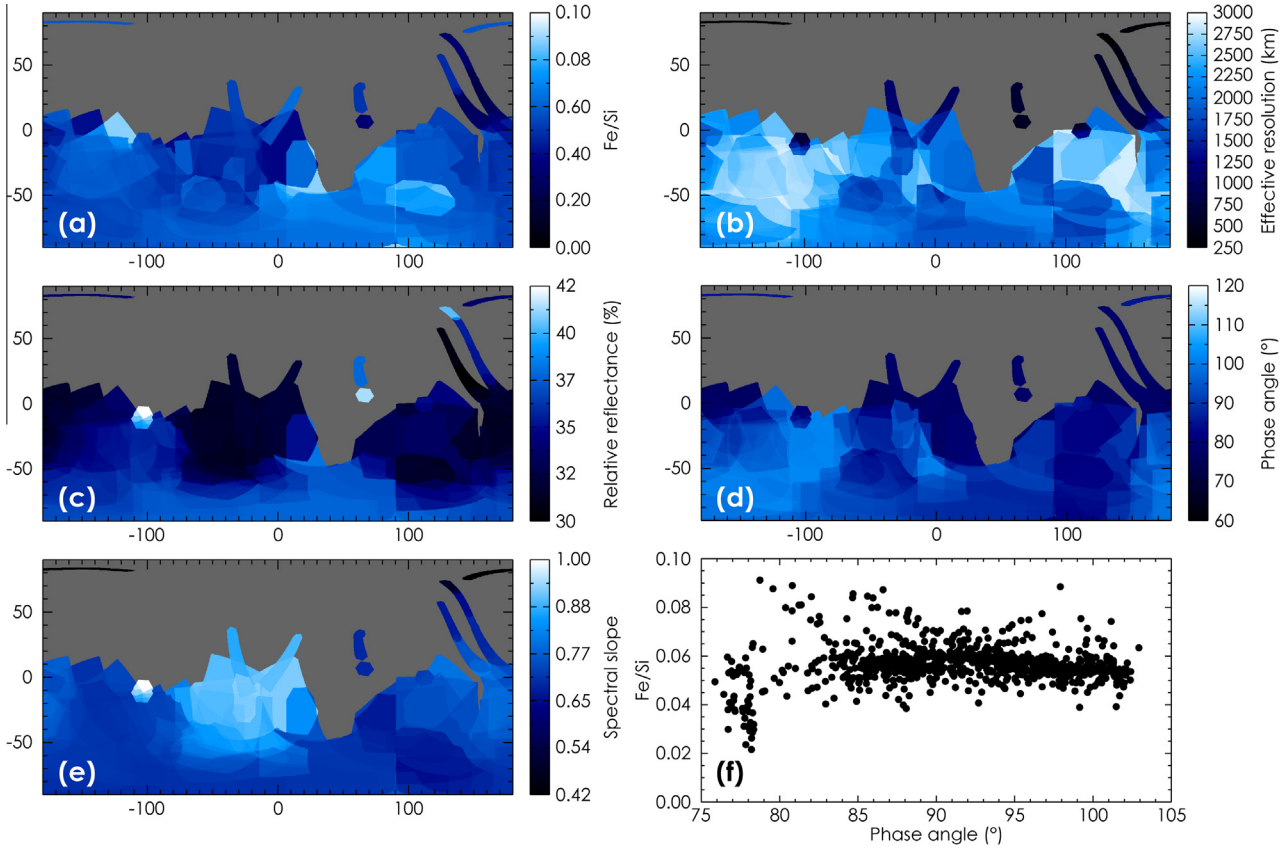

Fig. 9. Maps, in simple cylindrical projection, of (a) Fe/Si, (b) effective XRS spatial resolution, (c) smoothed spectral reflectance at 750 nm, relative to the maximum reflectance value for Mercury at this wavelength, (d) smoothed phase angle, and (e) smoothed spectral reflectance slope (ratio of reflectance at 430 to that at 1020 nm, wavelengths that span the range of the reflectance data). (f) Fe/Si versus phase angle for each pixel in the maps.

phase, such an arrangement could account for the absence of strong correlations between Fe/Si and the other elemental ratios we report (Fig. 7).

Another possible group of Fe-bearing minerals on Mercury's surface is the Fe-silicides. These phases form under extremely reducing conditions and have been found in aubrites (Casanova et al., 1993), for example, as perryite $(Ni,Fe)_5(SiP)_2$. Fe-silicides, e.g., fersilicite (FeSi), ferdisilicite ($FeSi_2$), and hapkeite (Fe_2Si), have also been detected in a lunar regolith breccia meteorite (Anand et al., 2004) and in an Apollo 16 regolith sample (Spicuzza et al., 2011), where they are thought to represent vapor-deposited material that results from micrometeoroid impacts.

The very low FeO contents predicted for silicates under the highly reducing conditions inferred for Mercury is also supported by the partial melting experiments on the enstatite chondrite meteorite Indarch (McCoy et al., 1999), which may be geochemically similar to Mercury's precursor materials (Nittler et al., 2011). These experiments produced three immiscible melts: Fe-rich metal, Fe-bearing sulfide, and silicate (containing very little Fe). However, if Indarch is indeed analogous to the materials that accreted to form Mercury, these experiments predict that the Fe-rich metal and sulfide melts should have segregated into the core during the planet's original differentiation. The mantle, from which later partial melts were derived to form the upper crust we observe, would have been almost entirely devoid of Fe (under the assumption that core formation was completely efficient). It is therefore surprising to detect Fe, even at the low levels indicated by the XRS and GRS data.

It is unlikely that the Fe we observe is a geologically recent exogenous coating from the deposition of Fe-rich meteoritic material, given that variations in Fe (and other elements) correlate strongly with the boundaries of geological units that are billions of years in age (e.g., those associated with the Caloris basin). The younger Caloris units (interior volcanic plains and exterior smooth plains; e.g., Denevi et al., 2013) have lower Fe/Si ratios than the older heavily cratered terrain, which could be evidence of meteoritic material accumulating on Mercury's surface over time. An analogous situation has been suggested to explain the correlation between the H content and age of geological units on asteroid 4 Vesta (Prettyman et al., 2012). However, we also observe a difference in the Fe/Si ratio between the circum-Caloris and Caloris interior smooth plains, which are more similar in age. In addition, the Fe/Si ratio of Mercury's surface is lower by a factor of ~25 than chondritic material. Mixing meteoritic material into Mercury's existing crust (at a level that can produce the observed Fe/Si ratios) is unlikely to cause the variations in other elemental ratios we detect, which correlate with the same geological boundaries.

We propose instead that the surface Fe content, and presumably the Fe content of the mantle source regions of the surface volcanic units, is the result of a "late veneer" of accreted material. Such a late veneer is analogous to that proposed for Earth to account for the abundances of highly siderophile elements in the terrestrial mantle (e.g., Morgan, 1986; Wang and Becker, 2013). Undifferentiated (i.e., Fe-bearing) material may have been added to Mercury following the principal period of core formation, but prior to the formation of much of the upper crust, which according to one model for the early impact flux at Mercury (Marchi et al., 2013) is dated at about 3.8–4.1 Ga. In this scenario, Mercury's mantle and crust would contain elevated abundances of highly siderophile elements (e.g., Re, Os, Pt). Such trace elements cannot be detected from orbit but would be a potential late veneer signature in rock samples from Mercury, which we may obtain in the future.

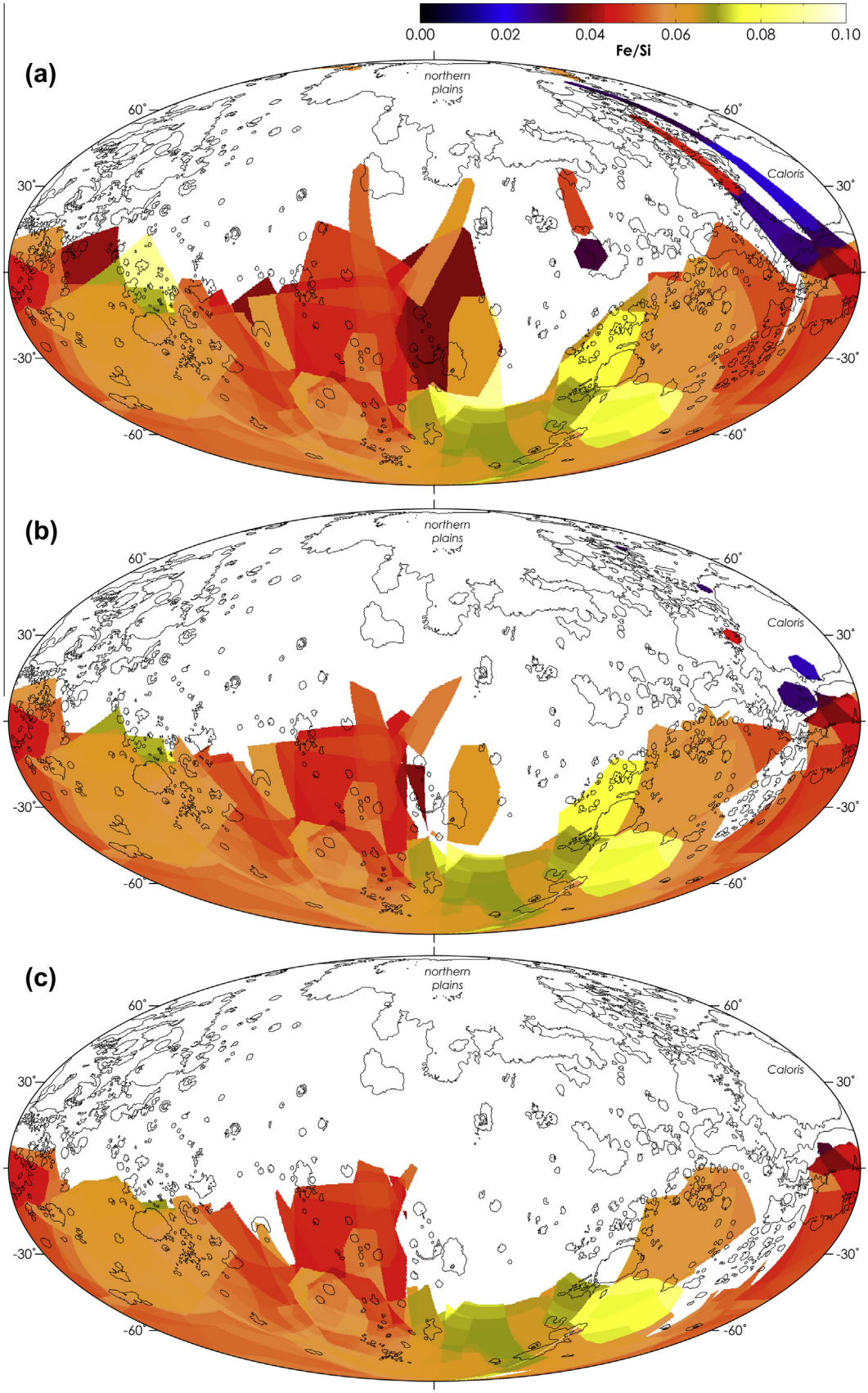

Fig. 10. Map of Fe/Si, corrected for phase angle, on the surface of Mercury (in a Mollweide projection centered on 0°E) derived from the 55 flare observations. See text for details of the map generation. The map in (a) includes all data for which Fe/Si information has been derived; the maps in (b) and (c) include only those pixels for which there are least two and three overlapping footprints, respectively. Smooth plains deposits, as mapped by Denevi et al. (2013), are outlined in black. Large-scale regions in the southern hemisphere with substantially lower (more red) and higher (more yellow) Fe/Si than the mean value (~0.06) can be identified in all three versions of the map.

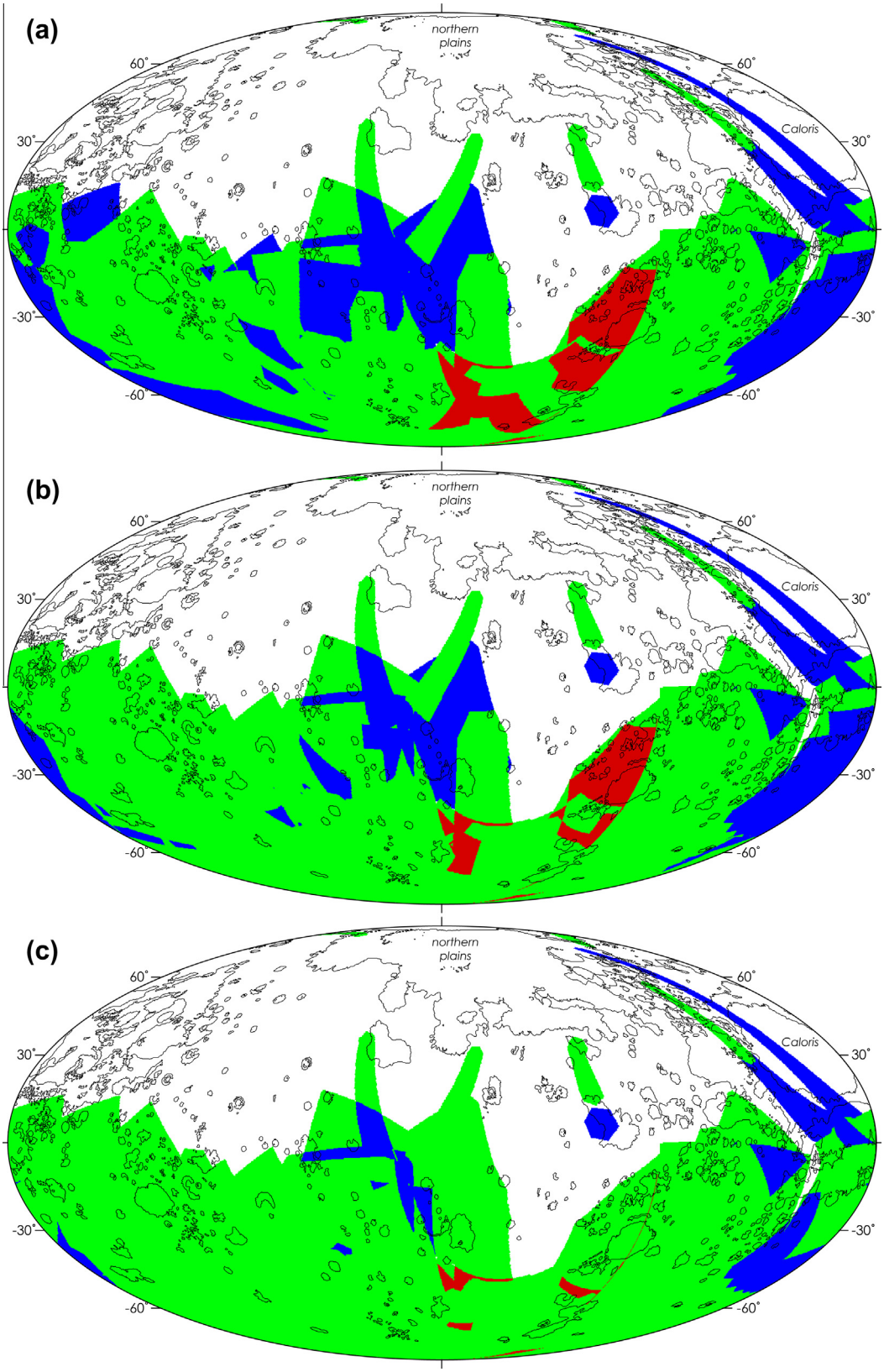

Fig. 11. Statistical significance of the observed surface Fe variations (see Fig. 9). Red and blue regions have an Fe/Si ratio that is at least (a) 2σ, (b) 2.5σ, or (c) 3σ above or below, respectively, the planetary average (green).

5.2. Role of Fe in Mercury's spectral reflectance

Mercury's surface reflectance spectra are generally flat and featureless (in the wavelength range 400–1000 nm), and the planet's terrains are characterized mainly by small differences in overall reflectance and spectral slope (Robinson et al., 2008; McClintock et al., 2008; Denevi et al., 2009; Blewett et al., 2013). However, low-Fe enstatite—the mineral thought to dominate Mercury's

surface (Nittler et al., 2011; Weider et al., 2012; Stockstill-Cahill et al., 2012; Charlier et al., 2013)—has a higher reflectance and steeper-sloped spectrum than Mercury's surface (Blewett et al., 2013). Given the substantial Na content of Mercury's surface (Peplowski et al., 2014), low-Fe olivine (forsterite) is likely to be an additional major mineral component (Stockstill-Cahill et al., 2012; Charlier et al., 2013), but its reflectance is also higher than that of the planet. A mixture of mafic silicate minerals (e.g., enstatite and forsterite) and a dark, red component is therefore required to match Mercury's spectrum. This latter phase is not thought to be Fe metal, because its steep spectral slope is dissimilar to the relatively shallow spectrum for the planet (Robinson et al., 2008).

Ilmenite ($FeTiO_3$), with its low reflectance and flat reflectance spectrum, was proposed as a potential darkening agent on Mercury (e.g., Denevi et al., 2009; Riner et al., 2009, 2010). However, the low Fe and Ti abundances reported here (Table 3), and by Nittler et al. (2011), rule out the possibility that ilmenite is a major mineral phase on Mercury's surface. Likewise, troilite has the appropriate spectral characteristics to account for aspects of Mercury's reflectance (Blewett et al., 2013), but the amount that can be present at the surface is limited by our results (see Section 5.1).

Laboratory reflectance spectra of oldhamite (CaS) indicate that the mineral is too bright to darken and redden Mercury's surface. Oldhamite also exhibits absorption features at ~500 and ~950 nm that are not observed in spectra of Mercury's surface. However, repeated heating of this material to Mercury daytime temperatures causes its spectral slope to decrease and absorption bands to weaken (Helbert et al., 2013). Nanophase opaque phases

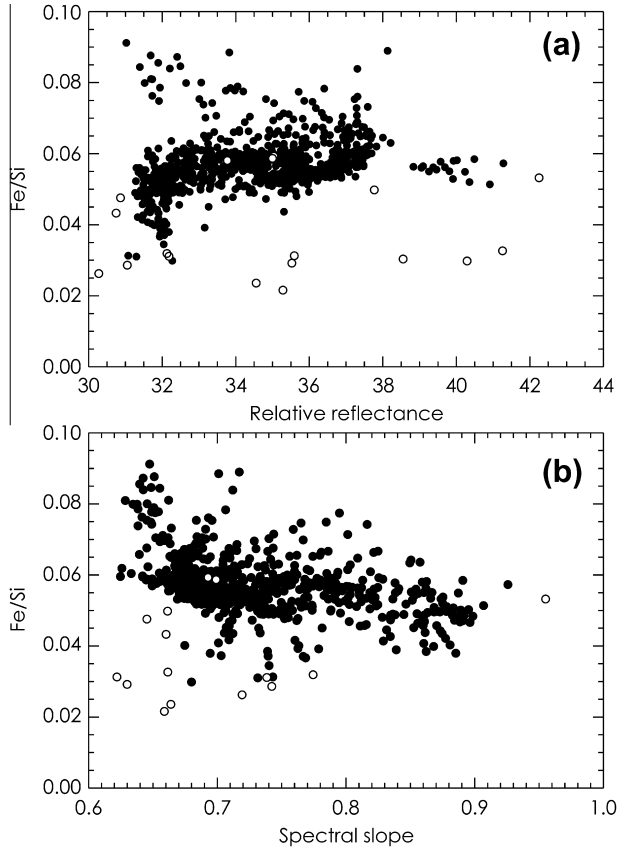

Fig. 12. Fe/Si ratio versus (a) relative reflectance at 750 nm, expressed as percentage of the maximum reflectance on Mercury at this wavelength and (b) the slope of the spectral reflectance (ratio of relative reflectance at 430 nm to that at 1020 nm). The values for each pixel in the Fe/Si map are divided into two groups according to the size of the footprints of the flare measurements from which they were derived; white and black points correspond to effective footprint resolutions of <1000 km and >1000 km, respectively.

(products of space weathering) can also darken, redden, and reduce the strength of absorption bands in reflectance spectra (e.g., Hapke, 2001; Noble and Pieters, 2003; Noble et al., 2007; Lucey and Noble, 2008; Lucey and Riner, 2011). Riner and Lucey (2012) concluded that the albedo variations among different terrains on Mercury, specifically high-reflectance red plains (HRP), intermediate terrain, and low-reflectance material (LRM) (Robinson et al., 2008), cannot be explained solely by the addition of an opaque mineral such as ilmenite or Fe metal. They showed that differential accumulation of space weathering products can account for the albedo differences, with the LRM containing the highest levels of these products and the HRP containing the least.

To investigate whether the large-scale variations in Fe/Si we observe are related to surface reflectance variations, we have plotted the Fe/Si values versus the relative reflectance at 750 nm and spectral slope (ratio of reflectance at 430 to that at 1020 nm) on a pixel-by-pixel basis in Fig. 12. We see neither a strong correlation between Fe/Si and relative reflectance (Fig. 12a) nor one between Fe/Si and spectral slope (Fig. 12b). If color differences among Mercury's terrains were caused primarily by variable Fe concentrations, we would expect to observe a positive correlation in Fig. 12b. The similar absence of correlations in the data from both the largest and smallest XRS footprints indicates that averaging our data over large regions does not necessarily prevent trends from being observed. Our results therefore show that differences in Fe can play only a minor role in causing the surface reflectance variations across Mercury's surface. Alternatively, if Fe-silicides (see previous section) are the main Fe-bearing phase and a major cause of impact darkening on Mercury's surface, reflectance variations connected to the presence of space weathering products may not correlate with changes in the Fe/Si ratio.

6. Conclusions

The analysis of 55 flare XRS measurements has provided estimates of the Fe/Si content and its spatial variation over Mercury's surface. These results are subject to a phase-angle effect, for which an empirical correction to the values has been made. The results confirm that the total Fe content of the surface is low, but there is resolvable heterogeneity across the planet. Large regions with an Fe content that is significantly different from the planetary mean are observed in the southern hemisphere, and there is evidence that many smooth plains deposits have a lower Fe/Si ratio than surrounding, older terrains. Fe on Mercury's surface is most likely contained as a minor component in sulfide phases, as Fe metal, or in Fe-silicides, rather than as ferrous Fe within mafic silicates. It is unlikely that Fe (within sulfide, metal, or silicate phases) plays a major role in producing the variations in surface reflectance that have been used to define Mercury's spectral terrain types.

There is evidence for an offset between the estimate of the Fe/Si ratio from XRS (mainly for the southern hemisphere) and from GRS (for the northern hemisphere). The reason for this offset remains unresolved, but it could be related to the empirical phase-angle correction for the XRS dataset and/or mineral mixing effects. We anticipate that the collection of further Fe measurements over Mercury's northern hemisphere during MESSENGER's second extended mission will provide a basis for further investigation of chemical heterogeneity in and around Mercury's volcanic smooth plains.

Acknowledgments

We thank the MESSENGER team for the development and operation of the MESSENGER spacecraft. We also thank two anonymous

reviewers for constructive comments. This work is supported by the NASA Discovery Program under contract NAS5-97271 to The Johns Hopkins University Applied Physics Laboratory and NASW-00002 to the Carnegie Institution of Washington.

References

Anand, M., Taylor, L.A., Nazarov, M.A., Shu, J., Mao, H.-K., Hemley, R.J., 2004. Space weathering on airless planetary bodies: Clues from the lunar mineral hapkeite. Proc. Natl. Acad. Sci. 101, 6847–6851.

Benz, W., Slattery, W.L., Cameron, A.G.W., 1988. Collisional stripping of Mercury's mantle. Icarus 74, 516–528.

Benz, W., Anic, A., Horner, J., Whitby, J.A., 2007. The origin of Mercury. Space Sci. Rev. 132, 189–202.

Blewett, D.T., Hawke, B.R., Lucey, P.G., 2002. Lunar pure anorthosite as a spectral analog for Mercury. Meteorit. Planet. Sci. 37, 1245–1254.

Blewett, D.T. et al., 2013. Mercury's hollows: Constraints on formation and composition from analysis of geological setting and spectral reflectance. J. Geophys. Res. Planets 118, 1–20. http://dx.doi.org/10.1029/2012/JE004174.

Casanova, I., Keil, K., Newsom, H.E., 1993. Composition of metal in aubrites: Constraints on core formation. Geochim. Cosmochim. Acta 57, 675–682.

Charlier, B., Grove, T.L., Zuber, M.T., 2013. Phase equilibria of ultramafic compositions on Mercury and the origin of the compositional dichotomy. Earth Planet. Sci. Lett. 363, 50–60.

Clark, P.E., Trombka, J.I., 1997. Remote X-ray spectrometry for NEAR and future missions: Modeling and analyzing X-ray production from source to surface. J. Geophys. Res. 102, 16361–16384. http://dx.doi.org/10.1029/97JE01086.

Denevi, B.W. et al., 2009. The evolution of Mercury's crust: A global perspective from MESSENGER. Science 324, 613–618.

Denevi, B.W. et al., 2013. The distribution and origin of smooth plains on Mercury. J. Geophys. Res. Planets 118, 1–17. http://dx.doi.org/10.1002/jgre.20075.

Dere, K.P., Landi, E., Mason, H.E., Monsignori Fossi, B.C., Young, P.R., 1997. CHIANTI: An atomic database for emission lines. Astron. Astrophys. Suppl. Ser. 125, 149–173.

Evans, L.G. et al., 2012. Major-element abundances on the surface of Mercury: Results from the MESSENGER Gamma-Ray Spectrometer. J. Geophys. Res. 117, E00L07. http://dx.doi.org/10.1029/2012JE004178.

Fegley Jr., B., Cameron, A.G.W., 1987. A vaporization model for iron/silicate fractionation in the Mercury protoplanet. Earth Planet. Sci. Lett. 82, 207–222.

Garcia, H.A., 1994. Temperature and emission measure from GOES soft X-ray measurements. Sol. Phys. 154, 275–308.

Hapke, B., 2001. Space weathering from Mercury to the asteroid belt. J. Geophys. Res. 106, 10039–10073.

Hauck II, S.A. et al., 2013. The curious case of Mercury's internal structure. J. Geophys. Res. Planets 118, 1–17. http://dx.doi.org/10.1002/jgre.20091.

Head, J.W. et al., 2011. Flood volcanism in the northern high latitudes of Mercury revealed by MESSENGER. Science 333, 1853–1856.

Helbert, J. et al., 2013. High-temperature spectroscopy of sulfides and implications for hollows on Mercury. Lunar Planet. Sci. 44. Abstract 1498.

Ho, G.C. et al., 2011. Observations of suprathermal electrons in Mercury's magnetosphere during the three MESSENGER flybys. Planet. Space Sci. 59, 2016–2025.

Klima, R.L. et al., 2013. Constraining the ferrous iron content of silicate minerals in Mercury's crust. Lunar Planet. Sci. 44. Abstract 1602.

Langevin, Y., 1997. The regolith of Mercury: Present knowledge and implications for the Mercury Orbiter mission. Planet. Space Sci. 45, 31–37.

Lawrence, D.J., Feldman, W.C., Goldsten, J.O., McCoy, T.J., Blewett, D.T., Boynton, W.V., Evans, L.G., Nittler, L.R., Rhodes, E.A., Solomon, S.C., 2010. Identification and measurement of neutron-absorbing elements on Mercury's surface. Icarus 209, 195–209.

Lewis, J.S., 1973. Chemistry of the planets. Annu. Rev. Chem. 24, 339–351.

Lucey, P.G., Noble, S.K., 2008. Experimental test of a radiative transfer model of the optical effects of space weathering. Icarus 197, 348–353.

Lucey, P.G., Riner, M.A., 2011. The optical effects of small iron particles that darken but do not redden: Evidence of intense space weathering on Mercury. Icarus 212, 451–462.

Marchi, S., Chapman, C.R., Fassett, C.I., Head, J.W., Bottke, W.F., Strom, R.G., 2013. Global resurfacing of Mercury 4.0–4.1 billion years ago by heavy bombardment and volcanism. Nature 499, 59–61.

Maruyama, Y., Ogawa, K., Okada, T., Kato, M., 2008. Laboratory experiments of particle size effect in X-ray fluorescence and implications to remote X-ray spectrometry of lunar regolith surface. Earth Planets Space 60, 293–297.

McClintock, W.E. et al., 2008. Spectroscopic observations of Mercury's surface reflectance during MESSENGER's first Mercury flyby. Science 321, 62–65.

McCoy, T.J., 1998. A pyroxene-oldhamite clast in Bustee: Igneous aubritic oldhamite and a mechanism for the Ti enrichment in aubritic troilite. Antarct. Meteorit. Res. 11, 32–48.

McCoy, T.J., Dickinson, T.L., Lofgren, G.E., 1999. Partial melting of the Indarch (EH4) meteorite: A textural, chemical, and phase relations view of melting and melt migration. Meteorit. Planet. Sci. 34, 735–746.

McCubbin, F.M., Riner, M.A., Vander Kaaden, K.E., Burkemper, L.K., 2012. Is Mercury a volatile-rich planet? Geophys. Res. Lett. 39, L09202. http://dx.doi.org/10.1029/2012GL051711.

Mittlefehldt, D.W., McCoy, T.J., Goodrich, C.A., Kracher, A., 1998. Non-chondritic meteorites from asteroidal bodies. Rev. Miner. 36, 4.1–4.195.

Morgan, J.W., 1986. Ultramafic xenoliths: Clues to Earth's late accretionary history. J. Geophys. Res. 91, 12375–12387.

Murchie, S.L. et al., 2008. Geology of the Caloris basin, Mercury: A view from MESSENGER. Science 321, 73–76.

Näränen, J., Parviainen, H., Muinonen, K., Carpenter, J., Nygård, K., Peura, M., 2008. Laboratory studies into the effect of regolith on planetary X-ray fluorescence spectroscopy. Icarus 198, 408–419.

Nittler, L.R. et al., 2001. X-ray fluorescence measurements of the surface elemental composition of Asteroid 433 Eros. Meteorit. Planet. Sci. 36, 1673–1695.

Nittler, L.R. et al., 2011. The major-element composition of Mercury's surface from MESSENGER X-ray spectrometry. Science 333, 1847–1850.

Noble, S.K., Pieters, C.M., 2003. Space weathering on Mercury: Implications for remote sensing. Sol. Syst. Res. 37, 31–35.

Noble, S.K., Pieters, C.M., Keller, L.P., 2007. An experimental approach to understanding the optical effects of space weathering. Icarus 192, 629–642.

Okada, T., 2002. Surface elemental composition of Asteroid 433 Eros: Discussions on the results of the NEAR/XGRS. Proc. 35th ISAS Lunar Planet. Symp., pp. 120–123.

Okada, T., 2004. Particle size effect in X-ray fluorescence at a large phase angle: Importance on elemental analysis of Asteroid Eros (433). Lunar Planet. Sci. 35. Abstract 1927.

Parviainen, H., Näränen, J., Muinonen, K., 2011. Soft X-ray fluorescence from particulate media: Numerical simulations. J. Quant. Spectrosc. Radiat. Transfer 112, 1907–1918.

Peplowski, P.N. et al., 2011. Radioactive elements on Mercury's surface from MESSENGER: Implications for the planet's formation and evolution. Science 333, 1850–1852.

Peplowski, P.N. et al., 2012a. Variations in the abundances of potassium and thorium on the surface of Mercury: Results from the MESSENGER Gamma-Ray Spectrometer. J. Geophys. Res. 117, E00L04. http://dx.doi.org/10.1029/2012JE004141.

Peplowski, P.N. et al., 2012b. Aluminum abundance on the surface of Mercury: Application of a new background-reduction technique for the analysis of gamma-ray spectroscopy data. J. Geophys. Res. 117, E00L10. http://dx.doi.org/10.1029/2012JE004181.

Peplowski, P.N., Evans, L.G., Stockstill-Cahill, K.R., Lawrence, D.J., McCoy, T.J., Nittler, L.R., Solomon, S.C., Sprague, A.L., Starr, R.D., Weider, S.Z., 2014. Enhanced sodium abundance in Mercury's north polar region revealed by the MESSENGER Gamma-Ray Spectrometer. Icarus 228, 86–95. http://dx.doi.org/10.1016/j.icarus.2013.09.007.

Prettyman, T.H. et al., 2012. Elemental mapping by Dawn reveals exogenic H in Vesta's regolith. Science 338, 243–246.

Riner, M.A., Lucey, P.G., 2012. Spectral effects of space weathering on Mercury: The role of composition and environment. Geophys. Res. Lett. 39, L12201. http://dx.doi.org/10.1029/2012GL052065.

Riner, M.A., Lucey, P.G., Desch, S.J., McCubbin, F.M., 2009. Nature of opaque components on Mercury: Insights into a mercurian magma ocean. Geophys. Res. Lett. 36, L02201. http://dx.doi.org/10.1029/2008GL036128.

Riner, M.A., McCubbin, F.M., Lucey, P.G., Taylor, G.J., Gillis-Davis, J.J., 2010. Mercury surface composition: Integrating petrologic modeling and remote sensing data to place constraints on FeO abundance. Icarus 209, 301–313.

Robinson, M.S. et al., 2008. Reflectance and color variations on Mercury: Regolith processes and compositional heterogeneity. Science 321, 66–69.

Schlemm II, C.E. et al., 2007. The X-Ray Spectrometer on the MESSENGER spacecraft. Space Sci. Rev. 131, 393–415.

Smith, D.E. et al., 2012. Gravity field and internal structure of Mercury from MESSENGER. Science 336, 214–217.

Solomon, S.C., 2003. Mercury: The enigmatic innermost planet. Earth Planet. Sci. Lett. 216, 441–455.

Solomon, S.C. et al., 2001. The MESSENGER mission to Mercury: Scientific objectives and implementation. Planet. Space Sci. 49, 1445–1465.

Spicuzza, M.J., Valley, J.W., Fournelle, J., Huberty, J.M., Treiman, A., 2011. Native silicon and Fe-silicides from the Apollo 16 lunar regolith: Extreme reduction, metal-silicate immiscibility, and shock melting. Lunar Planet. Sci. 42. Abstract 2231.

Sprague, A.L., Hunten, D.M., Lodders, K., 1995. Sulfur at Mercury, elemental at the poles and sulfides in the regolith. Icarus 118, 211–215.

Sprague, A.L., Emery, J.P., Donaldson, K.L., Russell, R.W., Lynch, D.K., Mazuk, A.L., 2002. Mercury: Mid-infrared (3–13.5 μm) observations show heterogeneous composition, presence of intermediate and basic soil types, and pyroxene. Meteorit. Planet. Sci. 37, 1255–1268.

Starr, R. et al., 2000. Instrument calibrations and data analysis procedures for the NEAR X-Ray Spectrometer. Icarus 147, 498–519.

Starr, R.D., Schriver, D., Nittler, L.R., Weider, S.Z., Byrne, P.K., Ho, G.C., Rhodes, E.A., Schlemm II, C.E., Solomon, S.C., Trávníček, P.M., 2012. MESSENGER detection of electron-induced X-ray fluorescence from Mercury's surface. J. Geophys. Res. 117, E00L02. http://dx.doi.org/10.1029/2012JE004118.

Stewart, S.T., Leinhardt, Z.M., Humayun, M., 2013. Giant impacts, volatile loss, and the K/Th ratios of the Moon, Earth, and Mercury. Lunar Planet. Sci. 44. Abstract 2306.

Stockstill-Cahill, K.R., McCoy, T.J., Nittler, L.R., Weider, S.Z., Hauck II, S.A., 2012. Magnesium-rich crustal compositions on Mercury: Implications for magmatism from petrologic modeling. J. Geophys. Res. 117, E00L15. http://dx.doi.org/10.1029/2012JE004140.

Trask, N.J., Guest, J.E., 1975. Preliminary geologic terrain map of Mercury. J. Geophys. Res. 80, 2461–2477.
Vilas, F., 1985. Mercury: Absence of crystalline Fe^{2+} in the regolith. Icarus 64, 133–138.
Vilas, F., 1988. Surface composition of Mercury from reflectance spectrophotometry. In: Vilas, F., Chapman, C.R., Matthews, M.S. (Eds.), Mercury. University of Arizona Press, Tucson, Ariz., pp. 59–76.
Wang, Z.C., Becker, H., 2013. Ratios of S, Se and Te in the silicate Earth require a volatile-rich late veneer. Nature 499, 328–331.
Weidenschilling, S.J., 1978. Iron/silicate fractionation and the origin of Mercury. Icarus 35, 99–111.
Weider, S.Z. et al., 2011. Planetary X-ray fluorescence analogue laboratory experiments and an elemental abundance algorithm for C1XS. Planet. Space Sci. 59, 1393–1407.
Weider, S.Z. et al., 2012. Chemical heterogeneity on Mercury's surface revealed by the MESSENGER X-Ray Spectrometer. J. Geophys. Res. 117, E00L05. http://dx.doi.org/10.1029/2012JE004153.
Zolotov, M.Y., Sprague, A.L., Hauck II, S.A., Nittler, L.R., Solomon, S.C., Weider, S.Z., 2013. The redox state, FeO content, and origin of sulfur-rich magmas on Mercury. J. Geophys. Res. Planets 118, 1–9. http://dx.doi.org/10.1029/2012JE004274.